University of Colorado
Boulder

CAPACITY SPECTRUM DESIGN APPROACH FOR HYBRID SLIDING-ROCKING POST-TENSIONED SEGMENTAL BRIDGES

by

SREENIVAS MADHUSUDHANAN

B.E., Sir M.Visvesvaraya Institute of Technology, 2011

A thesis submitted to the Faculty of Graduate School of the University of Colorado in partial fulfillment of the requirement for the degree of

Master of Science

Department of Civil, Environmental and Architectural Engineering

2016

This Thesis entitled:

Capacity Spectrum Design Approach for Hybrid Sliding-Rocking Post-Tensioned Segmental Bridges written by Sreenivas Madhusudhanan

Has been approved for the Department of Civil, Environmental and Architectural Engineering

_____

Professor Petros Sideris

_____

Professor Abbie Liel

_____

Professor Yunping Xi

Date: 7/28/2016

The final copy of this thesis has been examined by the signatories and we find that both the content and the form meet acceptable presentation standards of scholarly work in the above mentioned discipline

Sreenivas Madhusudhanan (M.S., Civil, Environmental and Architectural Engineering)

Capacity Spectrum Design Approach for Hybrid Sliding-Rocking Post-Tensioned Segmental Bridges

Thesis directed by Assistant Professor Petros Sideris

In this thesis a capacity spectrum method for hybrid sliding-rocking post-tensioned segmental bridges is proposed. A simplified model and two detailed models are derived for the conducting pushover analysis on the structure. The derived models are compared with experimental results and are used to conduct a parametric study of the design variables pertaining to hybrid sliding-rocking post-tensioned bridges. Next a capacity spectrum method for design is proposed which uses the detailed model. The proposed design method is then verified using nonlinear dynamic analysis on the structure using the detailed model for a given hazard. Results from the study show that the proposed Capacity spectrum design method predict the performance of the structure reasonably well when compared with nonlinear dynamic analysis.

Dedication

To my parents, grandparents, brother, the rest of my family and friends who have stood behind me.

Acknowledgements

I would like to express my appreciation and thanks to my advisor, Professor Petros Sideris, who provided me with the opportunity to work with him. He has been of immense help, advising and guiding me throughout my master's study. Discussion with him during the times of difficulties has put me back on my philosophical path of accomplishment. I also thank Professor Larry Esposito for the support and advising during my masters. I also thank LASP (Laboratory of Atmospheric and Space-Physics) for financial support during my masters.

I would also like to thank all the professors of the department of civil, Environmental and Architectural Engineering for their commitment to teach me during various academic courses that I took at the University of Colorado at Boulder.

Table of Contents

Figures

1. INTRODUCTION

1.1. General

In the U.S., many of the bridges are in immediate need of retrofit or replacement. In order to speed up this process, Accelerated Bridge Construction (ABC) techniques are actively researched. Precast concrete segmental construction are one of the ABC techniques. Several bridge substructure systems have been recently developed with improved seismic performance and construction rapidity. The majority of the systems researched over the years can be divided into (i) bents with prefabricated monolithic columns (without post-tensioning) connected with the bent cap and the foundation through rigid (or emulative of rigid) connections (Matsumoto et al. 2002; Hieber et al. 2005; Matsumoto et al. 2008; Pang et al. 2009; Stanton and Eberhard 2009; Steuck et al. 2009; Restrepo et al. 2011), and (ii) bents with segmental or prefabricated monolithic rocking columns incorporating internal unbonded post-tensioning (Hewes and Priestley 2002; Chou and Chen 2006; Hewes 2007; Restrepo et al. 2011; ElGawady and Dawood 2012) .These unbonded post-tensioning systems considerably increase the ductility capacity and self-centering capacity of bridge substructures.

A novel bridge substructure system was recently introduced by Sideris (Sideris 2012, Sideris et al. 2014b, Sideris et al. 2014c). The proposed system included substructure columns with unbonded post-tensioning, end rocking joints and intermediate sliding joints (or slip-dominant joints) along the height of the columns. Joint sliding provides energy dissipation with small damage and control of the applied seismic loading. Residual joint sliding is small and restorable after an intense earthquake event.

Force based seismic design of bridge systems incorporating HSR columns is difficult to apply. This is due to lack of a representative response modification factor R. In force based design, R-factors indirectly account for energy dissipation properties and ductility capacity of the system. For highly nonlinear systems such as HSR columns, these R factors are difficult to estimate (Priestley 1997) . For new systems, R factors can be estimated by using the procedure given in (FEMA 2009). However, the methodology mainly focusses on buildings.

Considering these shortcomings of force based designs, performance-based design methods such as direct displacement based design (DDSB) methods (Priestley et al. 2007) can be considered as alternative design procedure. The nonlinear properties of the system are incorporated in DDBD methods through an equivalent linearization obtained for a target design displacement. The major advantages of DDSB methods are

- Estimation of elastic period of the structure is not required.
- Primary design parameters are the deformations, which are representative measures of damage.
- Force reduction factors are not required for the design.
- System performance can be evaluated are various hazard levels.

Capacity spectrum methods (CSMs) are equivalent to the DDBD methods, and provide prediction of response variables for given hazard and a set of trial design/system parameters. A brief literature review of CSMs is described in the following section.

1.2. Literature review

CSM is a procedure that can be applied in the framework of Performance Based Seismic Design. The CSM was introduced initially in 1970s as a rapid evaluation procedure in a pilot project for

assessing seismic vulnerability of buildings at the Puget Sound Naval Shipyard (Freeman et al. 1975). In this procedure, the capacity of the structure is represented in the form of pushover curve. This curve is compared with the demand of the structure which is represented in the form of a response spectrum. The graphical intersection of the capacity curve and the demand curve provide the approximate response of the structure. To account for the inelastic response of the structure, the response spectra was reduced due to period lengthening. This was accounted based on the observations and studies of buildings and recorded building response (Czarnecki 1975, Freeman 1978 and Freeman et al. 1977). This procedure was used for several case-studies of buildings that had experienced ground motion (Freeman et al. 1976; Freeman et al. 1977, Freeman 1978, Freeman 1987). Several buildings were evaluated using CSM after the 1989 Loma Prieta earthquake in Mahaney et al. 1993 which also introduced the Sa versus Sd format for response spectra instead of Sa versus T. This procedure was incorporated in the *Seismic Design Guidelines For Essential Buildings Manual* (Freeman et al. 1984, Army 1986) as a design verification procedure for Army, Navy and Air force. Applied technology council (ATC) as a part of developing guidelines for seismic evaluation and retrofit of concrete buildings selected CSM as suggested procedure. In order to link the hysteretic damping to equivalent damping values, 3 categories of reduction factors were suggested. It was noticed by Krawinkler 1995 that a suitable value for equivalent viscous damping is difficult to ascertain since a stable relationship between hysteretic energy dissipation associated with the maximum excursion and equivalent viscous damping does not exist. Several methods were suggested to overcome this deficiency. FEMA 273 uses *Displacement Coefficient method*, where the demand is represented by inelastic displacement spectra which are obtained from elastic displacement spectra using a number of correction factors. Bertero 1995 recommended the use of smoothed inelastic design response spectra to represent the

demand. Chopra and Goel 1999 developed the *Capacity Demand Diagram Method* which uses a constant ductility design spectrum for the demand diagram. Most of the research conducted in Capacity spectrum method are applied to seismic assessment of buildings. Casarotti and Pinho 2007 developed an Adaptive Capacity spectrum method (ACSM), which was applied to bridge applications. It was noticed that the results of ACSM matched well with the dynamic analyses. The application of CSM for bridges was further verified by Pinho et al. 2007, where different CSM procedures were carried out on a wide set of bridge configurations. The research suggested that all the methods are able to predict displacement response with good accuracy. As the relationship between the demand and capacity can be visualized, CSM has added advantage compared to other PBSD methods. (Freeman 2004). The differences in the various methods of CSM mainly arise from the material behavior and the quantification of the energy dissipation. (Freeman 1998).

1.3. Objective and scope

The major objectives of this thesis are:

- Develop a model capable of performing quasi-static monotonic and cyclic pushover analysis of HSR columns.
- Verify the proposed model with experimental results
- Examine the key design variables of HSR columns using the proposed model
- Develop a capacity spectrum design procedure for HSR column that uses the proposed model.
- Verify the design from capacity spectrum method using nonlinear dynamic analysis of HSR column.

1.4. Arrangement of Thesis

This thesis consists of 4 chapters. Following this first introductory chapter, Chapter 2 discusses the proposed analytical models. This chapter also includes the results of parametric study conducted on the effect of major design variables on the response of HSR columns. In Chapter 3, a capacity spectrum design procedure for HSR columns is proposed. The proposed design method is verified with the results of incremental dynamic analysis. Finally, Chapter 4 presents a summary, major conclusion and scope for future work.

2. ANALYTICAL DERIVATION OF MONOTONIC AND CYCLIC PUSHOVER CURVES FOR HSR COLUMNS

In this section, a reference HSR column is presented. A *simplified* analytical model is proposed to compute the monotonic pushover curve for HSR columns. The simplified analytical model is implemented computationally to conduct pushover analysis. The results from the analysis is compared with experimental results. A *detailed* analytical model capable of conducting monotonic and cyclic pushover analysis is next derived. This detailed model is implemented computationally to conduct monotonic and cyclic pushover analysis. The results from the pushover analysis is then compared with experimental results. A parametric study is then conducted using the detailed model to assess the effect of design variables on the response of HSR columns.

2.1. Description of the HSR columns

HSR columns are post-tensioned segmental members consisting of two main components, HSR segmental joints and internal unbonded post-tensioned (PT) tendons. The segmental joints are friction type connections that mitigate seismic loading through joint sliding and joint opening (rocking). The joint sliding provides high energy dissipation with low damage due to the friction between the segments. The joint sliding also provides moderate self-centering due to shear resistance or the dowel effect of the PT tendons. The joint rocking on the other hand provides low energy dissipation and high self-centering. Energy dissipation with low damage are one of the salient features of bridges with HSR columns.

A reference HSR cantilever column is shown in Figure 1. All the joints except for bottom ones are designed such that they are allowed to slide and hence are called sliding-dominant (SD) joints. The bottom joint whose sliding is restrained is called as rocking-dominant (RD) joint. The sliding of

RD joints is restrained by either providing high coefficient of friction or by providing shear keys. In the vicinity of SD joints, the duct containing the PT tendons are replaced by tubing with larger diameter than that of duct. These are termed "duct adaptors" (Figure 1) and are used to control the response of SD joints. After the post-tensioning, the reference HSR cantilever column is subjected to a constant vertical force P_v, and a monotonically increasing lateral displacement u_h, associated with a horizontal force P_h. A typical response of the column to this loading is show in Figure 1 (a).

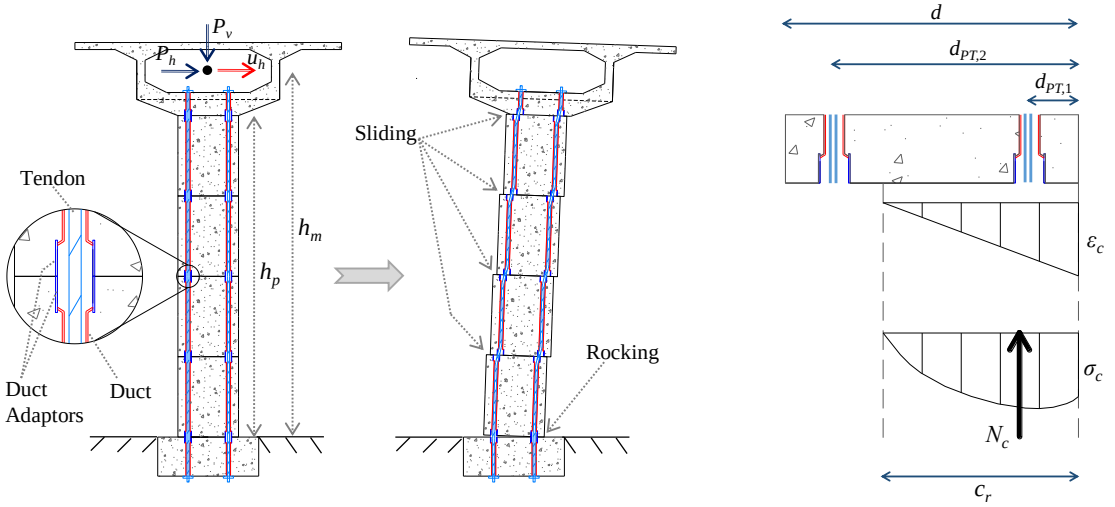

Figure 1: (a) Typical HSR-SD reference model and (b) Concrete stress and strain distribution at the bottom of a typical HSR-SD column.

2.2. Simplified analytical model

In this section a simplified model to compute the response of HSR columns subjected to monotonically increasing load is proposed. The discrete points of a pushover or moment curvature diagram is first computed. The pushover curve is assumed to be linear between these points to get a complete pushover curve. . Each stage in the pushover curve is quantified based on the strain experienced by the concrete cross-section. The distinct points or stages in the curve are (i) decompression, (ii) concrete proportionality limit, (iii) unconfined concrete strength, and (iv)

ultimate compressive strength of confined concrete. The stress and strain distribution at each stage is shown in Figure 2.

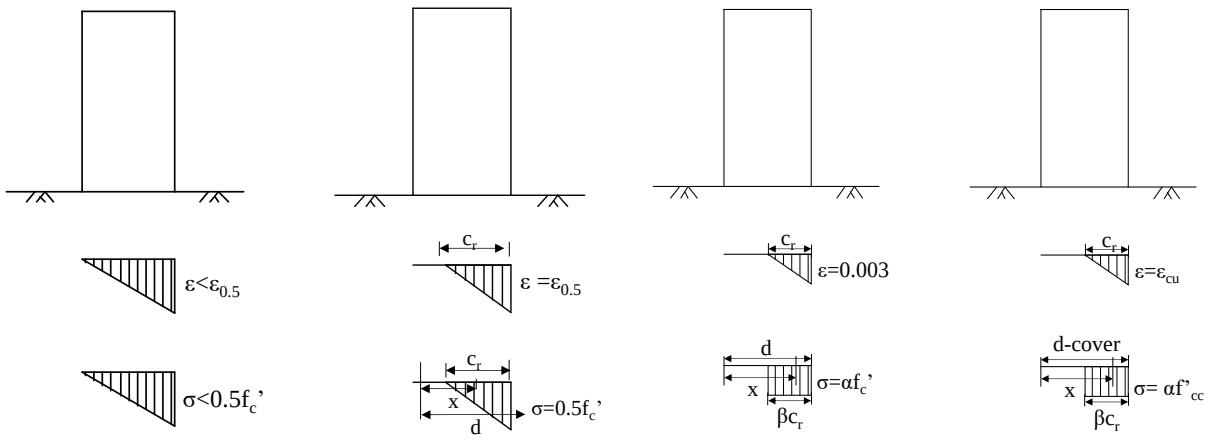

Figure 2: Stress distribution at various stages: (a) decompression stage, (b) concrete proportionality limit, (c) unconfined concrete strength, and (d) ultimate strain of confined concrete

2.2.1. Derivation

At each stage of the pushover curve the lateral force and displacement of the column is computed using a set of equilibrium and compatibility equations. The equilibrium at the bottom joint in the vertical direction is given as:

$$P_v + \sum N_{PT,i} = N_c \quad \textbf{(1)}$$

Here, P_v is the applied vertical load, $\Sigma N_{PT,i}$ is the sum of the forces of all the PT tendons shown in Figure 1 (a), and N_c is the resultant concrete force at the bottom shown in Figure 1 (b). The terms $\Sigma N_{PT,i}$ and N_c are computed separately for different stages in the curve discussed later in this section. The moment equilibrium at the bottom joint is given by:

$$h_m P_h + \left(\sum_j u_{sl,j} \right) P_v = M_c + M_{PT} \quad \textbf{(2)}$$

Here, the term $\left(\sum_j u_{sl,j}\right)P_v$ is the moment due to vertical force P_v resulting from the secondary effect due to sliding in all the joints $\left(\sum_j u_{sl,j}\right)$, M_c is the moment resistance due to concrete, M_{PT} is the moment resistance due to the unbonded post-tensioning and P_h is the horizontal force applied at a height h_m, where h_m is the center of mass of the superstructure.

For a given strain ε_c and contact length c_r (< d), as shown in Figure 2 (b), the concrete axial force including confinement effects can be obtained using the equivalent stress block method by (Paulay and Priestley 1992) as:

$$N_c = (\alpha_{cc} f'_{cc})(\beta_{cc} c_r) b_w \quad \textbf{(3)}$$

where, b_w is the width of the cross-section, α_{cc} and β_{cc} are the stress block parameters obtained from Figure 3, f'_{cc} is the strength of the confined concrete obtained from (Mander et al. 1988) and ε_{cc} is corresponding strain at f'_{cc} discussed in the next section.

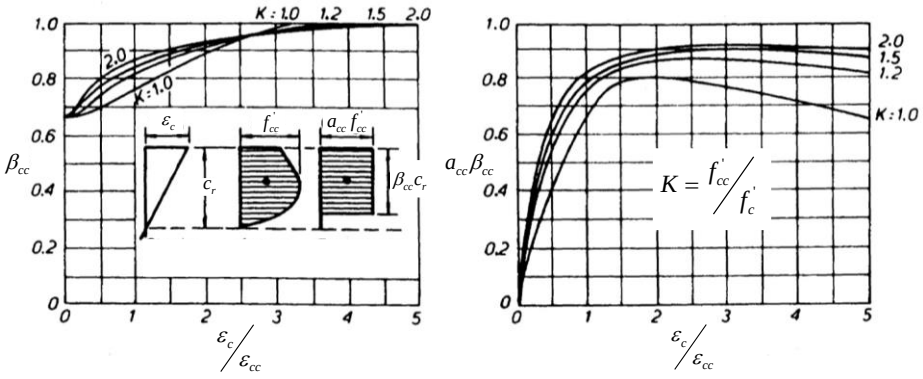

(a) **(b)**

Figure 3: Stress block parameter for any given strain, ε_c, from (Paulay and Priestley 1992)

Similarly, the moment resistance due to concrete is given as:

$$M_c = \left(\frac{d}{2} - \frac{\beta_{cc} c_r}{2} \right) (\alpha_{cc} f'_{cc})(\beta_{cc} c_r) b_w \quad \textbf{(4)}$$

where d is the total depth of the concrete cross-section. Note that Figure 3 permits use of the equivalent stress block method for any strain, ε_c, and for both the confined and unconfined concrete.

When the maximum concrete stress is smaller than 0.5fc', the stress distribution over the joint can be assumed to be linear and the total concrete force is computed using the analytical integration given in (5), instead of the equivalent stress block method (equation (3) and (4)). In that case, the total concrete force can be computed by analytical integration as:

$$N_c = \int_A \sigma(x)\, dA \quad \textbf{(5)}$$

Where $\sigma(x)$ is the value of the concrete stress at distance x from the reference axis.

Similarly, the concrete moment resistance in that case is given as:

$$M_c = \int_A x\sigma(x)\, dA \quad \textbf{(6)}$$

For a given concrete compressive strain and as long as joint opening occurs (i.e., $c_r < d$), the rocking rotation at the bottom, θ_r, can be obtained by the following compatibility equation:.

$$\theta_r = l_r \phi_r = l_r \left(\frac{\varepsilon_c}{c_r} \right) \quad \textbf{(7)}$$

where ϕ_r is the rocking curvature at the bottom joint, and l_r is the equivalent hinge length. Different researchers have suggested different values for equivalent hinge length. Different values of l_r are considered at different deformation stages, such as $l_r = 5.25\, c_r$ for $\varepsilon_c = 0.003$ (Harajli 2010), and l_r

= c_r for $\varepsilon_c = \varepsilon_{cu}$ (Restrepo and Rahman 2007), where ε_{cu} is the ultimate strain of confined concrete. If no gap opening occurs (i.e., $c_r = d$), then $\theta_r = 0$.

The extension of the *i*-th tendon which is located at a distance $d_{PT,i}$ from the end compression fiber is given as (Sideris 2012; Sideris et al. 2014b; c):

$$u_{PT,i} = \underbrace{\theta_r \left(d_{PT,i} - c_r \right)}_{\text{Due to rocking at bottom}} + \underbrace{\sum_j 2h_{da} \left(\frac{1}{\cos \psi_j} - 1 \right)}_{\text{Due to joint sliding}} \quad \textbf{(8)}$$

Where, ψ_j is the tendon deviation angle due to sliding at the *j*-th joint and is given as:

$$\tan \psi_j = \frac{\left\langle \left| u_{sl,j} \right| - u_{sl,b} \right\rangle}{2h_{da}} \operatorname{sgn}\left(u_{sl,j} \right) \quad \textbf{(9)}$$

Where $< u >$ are the Macauley brackets ($< u > = u$ for $u > 0$ and $< u > = 0$ otherwise), $u_{sl,j}$ is the current sliding at the j-th joint (with $|u_{sl,j}| \leq D_{da}$-D_{PT}, where D_{da} = duct adapter diameter, and D_{PT} = diameter of the PT tendon) and $u_{sl,b}$ is the sliding amplitude at which the bearing contact between the duct and the tendon initiates. Note that for all SD joints, $u_{sl,b} = D_d$-D_{pt}, where D_d is the diameter of the duct.

Assuming that all tendons have the same geometric and material properties, the force at the i-th tendon is given as:

$$N_{PT,i} = N_{PTo,i} + \frac{E_{PT} A_{PT}}{L_{PT}} u_{PT,i} \leq f_{PT,y} A_{PT} \quad \textit{and} \quad N_{PT,i} \geq 0 \quad \textbf{(10)}$$

where $N_{PTo,i}$ is the initial post-tensioning force of the *i*-th tendon, E_{PT} is the Young's modulus of the tendon, A_{PT} is the cross-section area of the tendon, L_{PT} is the length of the tendon, and $f_{PT,y}$ is the yield stress of the tendon. The total force of the unbonded tendons is given as:

$$N_{PT} = \sum_i N_{PT,i} \tag{11}$$

The corresponding moment due to the unbonded tendons is given as:

$$M_{PT} = \sum_i \left(d_{PT,i} - \frac{d}{2} \right) N_{PT,i} \tag{12}$$

At a given deformation stage, the corresponding lateral displacement is given as:

$$u_h = \underbrace{\left(\frac{h_p^3}{3EI} + \frac{h_p^2 \left(h_m - h_p \right)}{2EI} \right) P_h}_{\text{Displacement due to lateral load}} + \underbrace{\left(\frac{h_p \left(h_m - h_p \right)}{EI} + \frac{h_p}{2EI} \right) P_h \left(h_m - h_p \right)}_{\text{Rigid body rotation effect}} + \left(h_m - \frac{l_r}{2} \right) \theta_p + \sum_j u_{sl,j} \tag{13}$$

where h_p is the height of the deformable part of the column, E is young's modulus of the concrete and I is the moment of inertia of the column cross-section. The first term corresponds to the elastic response of the column, the second term corresponds to the rigid body rotation and translation of the cap beam and superstructure as a result of the elastic translation and rotation of the top end of the column, the third term corresponds to the displacement of the center of mass of the superstructure resulting from rigid body rotation due to rocking at the bottom, and the fourth term represents the displacement due to sliding at all SD joints. Next each stages considered in the pushover curve for a HSR RD and HSR SD column is separately discussed.

2.2.2. Rocking column without joint sliding

The response of a rocking column assumes that the sliding remains zero at all the stages of pushover curve (i.e., $u_{sl,j} = 0$ and $\psi_j = 0$ for all j). The different stages considered in a pushover curve of rocking column without joint sliding is given below.

- Decompression Stage

Decompression (Figure 2 (a)) is assumed to occur at low stresses (linear response). By setting the stress and strain at the tensile fiber equal to zero and using the expressions for elastic response for finding N_c and M_c (using equations (5) and (6)), the lateral force and displacement are computed using equations (2) and (13). The stress in the compression fiber is computed such that it satisfies the vertical equilibrium condition given in equation (1). If the resulting stresses are found to exceed $0.5f'_c$, the "stress-block" method (using equations (3) and (4)) should be used to find N_c and M_c. Different values of σ_c are selected until equilibrium and compatibility equations are satisfied.

- Concrete Proportionality Limit

The proportionality limit refers to the transition from the linear elastic response to the nonlinear response. This transition is assumed to take place at 50% of the nominal concrete compressive strength, f'_c. Assuming that the stress equals $0.5f'_c$ at the end compressive fiber (Figure 2 (b)), the value of c_r is chosen such that equilibrium and compatibility equations are satisfied. The concrete proportionality limit is usually reached after some joint opening has occurred.

- Unconfined Compressive Strength

The unconfined compressive strength is reached when the strain at the extreme fiber reaches 0.003. Confinement effects are neglected in this stage ($f'_c \approx f'_{cc}$, $a_{cc} \approx 0.85$, $\beta_{cc} \approx 0.85 - 0.05 < f'_c$ (ksi) - 4 ksi$\geq$0.65). The value of c_r are selected (for the given ε_c = 0.003) such that the equilibrium and compatibility equations are satisfied.

- Ultimate Compressive Strength of Confined Concrete

The ultimate compressive strain of the confined concrete occurs when the hoop reinforcement provided in the concrete segment fractures. This strain is given as (Paulay and Priestley 1992):

$$\varepsilon_{cu} = 0.004 + \frac{1.4\rho_s f_{yh}\varepsilon_{sm}}{f_{cc}'} \leq 0.02 \quad \textbf{(14)}$$

where ρ_s is the volumetric ratio of transverse steel is, f_{yh} is the yield stress of the hoop reinforcement. ε_{sm} is the steel strain at maximum tensile stress (≈ 0.15 for Grade 40 and 0.10 for Grade 60 rebar) and f_{cc} is the compressive strength of the confined concrete. For a rectangular column with different transverse reinforcements in two different directions (shown in Figure 4 (a)), the lateral confining pressure are separately computed in two directions. The confinement effectiveness ratio is computed using the equation given below (Mander et al. 1988)

$$k_e = \frac{\left(1 - \sum_{i=1}^{n} \frac{(w_i')^2}{6b_c d_c}\right)\left(1 - \frac{S'}{2b_c}\right)\left(1 - \frac{S'}{2d_c}\right)}{(1 - \rho_{cc})} \quad \textbf{(15)}$$

where w'_i is the ith clear distance between adjacent longitudinal bars as show in Figure 4 (a). b_c and d_c are the core dimension to centerlines of perimeter hoop in x and y directions and S' is the clear vertical spacing between spiral or hoop bars. The lateral confining stress on concrete in x and y direction (f_{lx} and f_{ly}) is given as:

$$f_{lx} = \rho_x f_{yh}$$
$$f_{ly} = \rho_y f_{yh} \quad \textbf{(16)}$$

where ρ_x and ρ_y are the transverse reinforcement ratios in x and y direction respectively. f_{yh} is the yield strength of the transverse reinforcements. To find the compressive strength of confined concrete, the confined strength ratio is obtained for the computed value of f_{lx} and f_{ly} using the plot given in figure Figure 4 (b). The corresponding strain at confinement is given as:

$$\varepsilon_{cc} = 0.002\left(1+5\left(\frac{f'_{cc}}{f'_{c}}-1\right)\right) \quad \textbf{(17)}$$

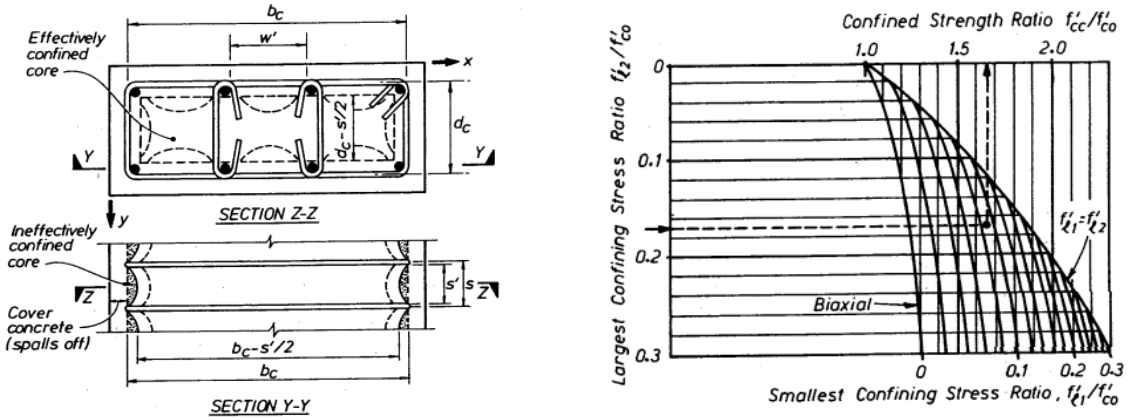

(a) **(b)**

Figure 4 (a) Effective confined core for rectangular hoop reinforcement (b) Confined strength determination from Lateral confining stresses for rectangular sections (Mander et al. 1988; Paulay and Priestley 1992)

Once the f_{cc}, ε_{cu} and ε_{cc} is obtained from the above equations, the value of c_r is computed such that the equilibrium and compatibility condition is satisfied. A typical force vs. displacement response of a rocking-only column is given in Figure 5.

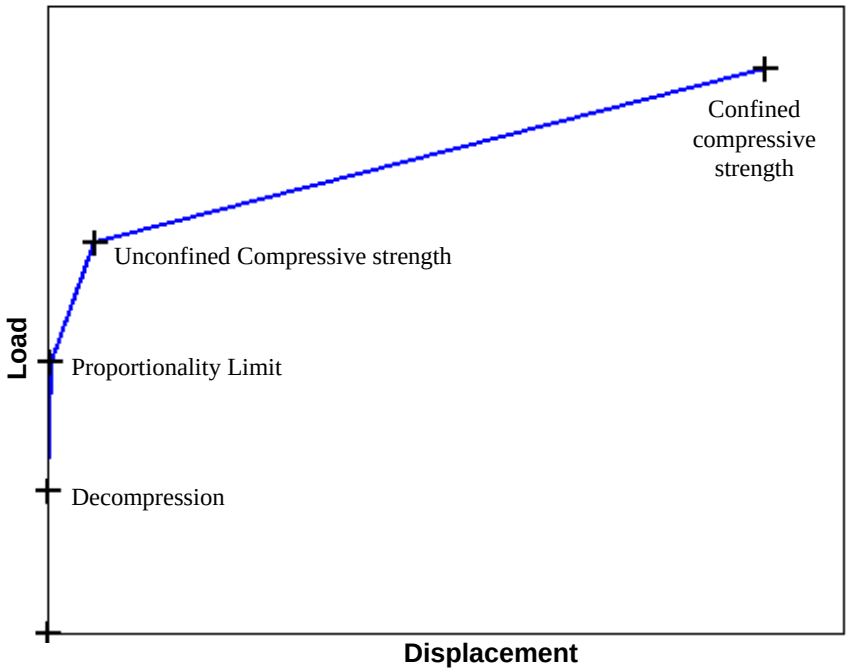

Figure 5: Force vs. displacement response of rocking-only column.

2.2.3. Rocking column with joint sliding (HSR Column)

For an HSR column, joint sliding initiates (by design) before the strength of the unconfined concrete (ε_c = 0.003) has been reached at the bottom joint. Also, sliding is designed to reach its maximum at all joints before the ultimate strain of the confined concrete has been reached. Furthermore, for economical designs, the decompression (and/or concrete proportionality limit) may occur before sliding initiation.

For an HSR column, the following distinct stages are considered: (i) Decompression, (ii) Concrete Proportionality limit, (iii) Sliding Initiation, (iv) End of sliding at each SD joint, (v) Ultimate strain of confined concrete after sliding has been reached at all SD joints, and (vi) Complete Unloading.

The stages of decompression and concrete proportionality limit are evaluated as described for the rocking column. If joint sliding initiates before the concrete proportionality limit stage, the concrete proportionality limit stage is dropped. Also, if joint sliding initiates before the

decompression stage, both the decompression stage and the concrete proportionality limit stage are dropped. For evaluation of the force vs. displacement at different stages, Eqs. (1) to (13) are considered.

- Initiation of sliding

The joint sliding initiates when the lateral force, P_h, becomes equal to the shear resistance of the SD joints. For Coulomb friction, this condition becomes:

$$P_h = \mu N_c \quad \textbf{(18)}$$

Here, all joints are assumed to have the same friction coefficient and the axial force is assumed to be constant throughout the height of the column. In this stage, a compressive strain ε_c, is first selected. For this value of strain, the c_r satisfying the equilibrium and compatibility is found. For the resulting values of P_h and N_c, Eq. (18) is examined. If Eq. (18) is not satisfied, then a different value of ε_c is selected. This strategy continues a value of ε_c that satisfies Eq. (18) is found. Note that for this stage, $u_{sl,j} = 0$ and $\psi_j = 0$ for all j.

- End of Sliding at each Slip-dominant joint

Sliding at the j-th joint ends when the external lateral force, P_h, is in equilibrium with the frictional resistance and the tendon bearing resistance at that joint, as expressed by the following equation:

$$P_h = \mu N_c + N_{PT} \sin(\psi_j) \quad \textbf{(19)}$$

It is assumed that the sliding ends at one joint before sliding begins at the next joint. For the computation of the total post-tensioning force, the tendon extension due to sliding at the current joint and joints that have experienced joint sliding earlier is considered. For the first joint, $u_{sl,j}$ (with $j = 1$) is set equal to its maximum value, while $u_{sl,j} = 0$ for all other joints. Then, a value of the compressive strain, ε_c, is selected. For this value, the value of c_r is computed to satisfy the

equilibrium and compatibility conditions. For the resulting values of P_h, N_c, and N_{PT}, Eq. (19) is examined. If Eq. (19) is not satisfied, then a different value of ε_c is selected. This strategy continues a value of ε_c that satisfies Eq. (19) is identified. For the end of sliding at the second joint, $u_{sl,j}$ at both the first and second joint (j = 1 and 2) receives its maximum value, while sliding is set to zero in the rest of the SD joints. Then, a value of the compressive strain, ε_c, is identified for which Eq. (19) is satisfied. The same procedure is repeated until sliding at all joints is completed.

- Ultimate Strain of Confined Concrete after Sliding Completion at all Slip-dominant Joints

This response stage is similar to the corresponding stage of the rocking column. However, it considered that the sliding, $u_{sl,j}$, has been completed at all SD joints contributing to the tendon extension and the equilibrium and compatibility equations. In this stage, the value of c_r is selected, for the given $\varepsilon_c = \varepsilon_{cu}$ and for $u_{sl,j}$ = max at all SD joints) until equilibrium and compatibility is satisfied.

- Complete Unloading

The damage to the column due to rocking at the bottom is assumed small and is neglected. Thus, upon removal of the horizontal load, P_h, residual rocking is zero. However, residual joint sliding cannot be neglected because the dowel effect of the tendons is not sufficient to provide complete sliding self-centering. The residual sliding will be the same at all joints and can be obtained when the following condition is satisfied:

$$\mu N_c = N_{PT} \sin \psi_j \quad \textbf{(20)}$$

This condition is obtained from equation (19) by setting P_h = 0 and considering reversal of the friction force. In order to find the residual displacement, the value of $u_{sl,j}$ is varied. As a result, ψ_j is varied (through Eq.(9)) and N_{PT} is varied (through Eq. (8)). The value of $u_{sl,j}$ (same for all j)

satisfying the equilibrium (equation (20)) will be the residual joint sliding when the horizontal load is completely removed ($P_h = 0$). For unloading after sliding has been completed for some of the joints, the same approach is followed. However, in the computation of N_{PT} (through Eqs. (8) and (10)), only the joints that have completed their sliding are included. A pushover curve for a typical HSR-SD column is shown in Figure 6. Each point in the pushover curve after the sliding initiation represents the end of sliding in SD joints. The point corresponding to joint 5 is the stage where the maximum sliding is achieved in all the SD joints. To predict the hysteretic behavior of the curve, unloading in this model is assumed to follow the same path as that of loading point till the point corresponding to end of sliding at joint 5. After this, the pushover curve is assumed to vary linearly connecting the end of sliding point. The area enclosed by the loading and unloading curve represents that energy dissipated due to joint sliding.

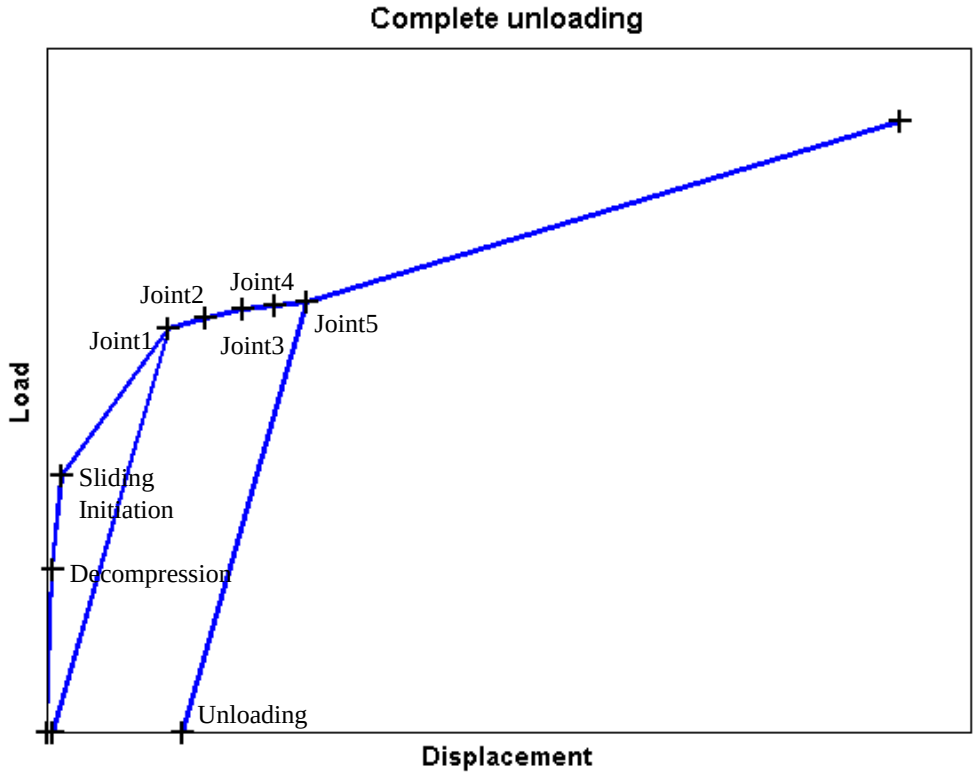

Figure 6: Typical Load vs. displacement curve of HSR-SD column.

2.2.4. Computational implementation

In this section, the computational implementation of the simplified model is discussed. The solution strategy for each stage of pushover for rocking-only and HSR columns is discussed separately. For both the pushover curves, the cross sectional area between the tension fiber and compression fiber is divided into small areas. The concrete reaction force N_c is then computed using numerical integration of the areas and the stress based on the stress distribution for the given stage.

2.2.4.1. Computational implementation for rocking-only columns

- Decompression Stage

In this stage, the primary unknown is the stress σ_c at the compression fiber. A bisection method algorithm is used to find the of σ_c (i.e., the solutions), that satisfies the equilibrium and compatibility equations. The steps in bisection algorithm is given below.

i. Find stresses σ_a and σ_b such that $\sigma_a < \sigma_b$ and $f(\sigma_a).f(\sigma_b) < 0$, where $f(\sigma_a)$ and $f(\sigma_b)$ is defined as the difference of the LHS from the RHS of equation (1) computed for σ_a and σ_b.

ii. Find $\sigma_m = \dfrac{\sigma_a + \sigma_b}{2}$

iii. If $\left| f\left(\sigma_m\right)\right| < tolerance$, then σ_m is the solution. Compute the horizontal force and lateral displacement for this strain.

iv. If $\left| f\left(\sigma_m\right)\right| > tolerance$ and $f\left(\sigma_m\right).f\left(\sigma_b\right) < 0$, then $\sigma_a = \sigma_m$

v. Otherwise, If $\left| f\left(\sigma_m\right)\right| > tolerance$ and $f\left(\sigma_m\right).f\left(\sigma_a\right) < 0$, then $\sigma_b = \sigma_m$

vi. Go back to step ii.

Repeat this process until $\left| f\left(\sigma_m\right)\right| < tolerance$.

- Proportionality limit Stage

In this stage the primary unknown to be solved is c_r. The stress in the extreme compression fiber is taken as $0.5f'_c$. Bisection method discussed in previous section is used to find c_r that satisfies the equilibrium condition given in equation (1).

- Unconfined Compressive Strength

The method of finding c_r is similar to that of the previous stage. However, equivalent stress block method is used to find the stress distribution across the cross section.

- Ultimate Compressive Strength of Confined Concrete

Similar to the previous stage c_r is the primary unknown to be solved. Ultimate compressive strength and the stress block parameters of confined concrete is computed using the equations (14) to (17) and using Figure 3 (a) and (b).

2.2.4.2. Computational implementation for HSR column

The evaluation of the decompression and proportionality limit stages are similar to that of HSR-RD column. The computational implementation of other stages is given below.

- Initiation of sliding

In this stage, the strain ε_c which satisfies the equilibrium condition given in equation (18) is computed. At each guess of strain, another bisection algorithm is implemented to find the right c_r that satisfies the equilibrium condition given in equation (1). The resulting c_r is used to find P_h and N_c which is then used to evaluate equation (18).

- End of Sliding at each Slip-dominant joint

In this stage, the end of sliding at each SD joint is evaluated separately. At each point, one of the SD joint reaches its maximum. Similar to the previous stage, strain ε_c which satisfies the equilibrium condition given in equation (19) is computed. A bisection algorithm to find the right strain is used. At each guess of strain, another bisection algorithm to find c_r that satisfies the equilibrium condition given in equation (1) is implemented. The resulting c_r is used to find P_h, N_c and N_{PT} which is then used to evaluate equation (19).

- Ultimate Strain of Confined Concrete after Sliding Completion at all Slip-dominant Joints

Evaluation of this stage is similar to the ultimate strain of confined concrete for rocking-only column. The sliding at all the joints is set to its maximum and stress block parameters of confined concrete is computed. A bisection method is then used to compute c_r that satisfies the equilibrium condition given in equation (1).

- Complete Unloading

The primary unknown in this stage is $u_{sl,j}$, this value is varied such that the equilibrium condition given in equation (20) is satisfied. Bisection method is used to find $u_{sl,j}$, that satisfies equation (20).

2.2.5. Validation of Simplified Method

In this section, the proposed model is compared with the test data from quasi-static cyclic testing on HSR columns as part of an extensive experimental program that also included shake tables testing of a large-scale single-span bridge specimen (Sideris 2012; Sideris et al. 2014b; c). The specimen included a box-girder segmental superstructure and two piers (see Figure 7(a)). Each pier included a five-segment HSR column with hollow square cross section and a cap beam of trapezoidal solid section (see Figure 7(b) and (c)). The box girder included #3 hoop reinforcements

provided in 3" spacing, The PT system included eight straight internal unbonded tendons of diameter of 0.6 inches and initial post-tensioning of 20 kips per tendon. The ducts had interior diameter of 0.9 inches. The duct adaptors had interior diameter D_{da} = 1.375 inches and height h_{da} =1.5 inches. A thin layer of silicon material was applied at the interface of all pier joints to achieve a target coefficient of friction in the range of 0.08 to 0.1. For loading in the lateral direction, h_m = 158 inches, while h_p = 120 inches (per Figure 7(a)). The specimen was subjected to a quasi-static cyclic loading. The resultant pushover curve is compared with the results of the proposed simplified model.

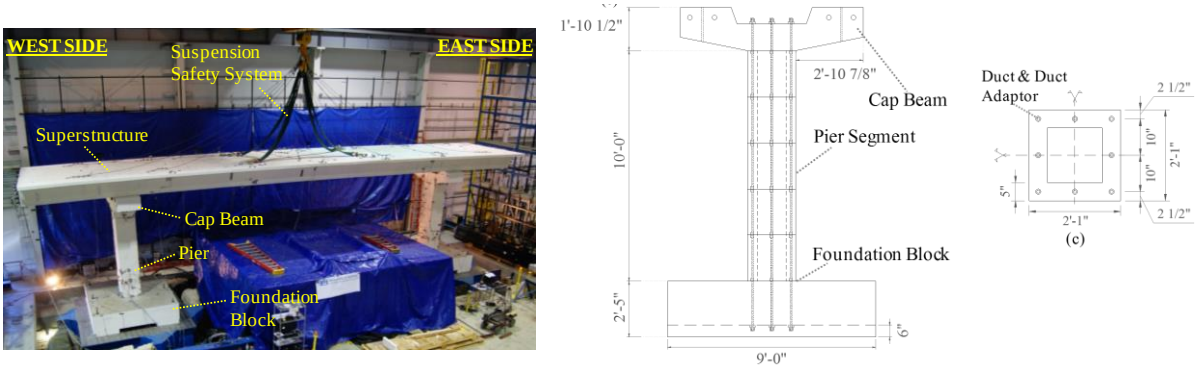

(a) **(b)** **(c)**

Figure 7:(a) Photo of the test specimen, (b) substructure column, and (c) column cross-section

Figure 8 given below shows the comparison between the two pushover curves. It can be noted from Figure 8 (a) that the peak horizontal force is predicted reasonably well. After the unloading begins, the displacement corresponding to zero horizontal force is the residual displacement. It can be seen from the Figure 8 (b) that the residual displacements are under-predicted. One of the main reasons for under-predicting the peak displacement is due to the fact that the experiment conducted was a continuous cyclic pushover test with increasing amplitude in each cycle. Due to the damage in concrete in previous cycles, the stiffness properties of the structure may have changed.

Moreover, the fact that friction between tendons and ducts has not been considered in the model has also contributed to the lower residual displacements predicted by the model.

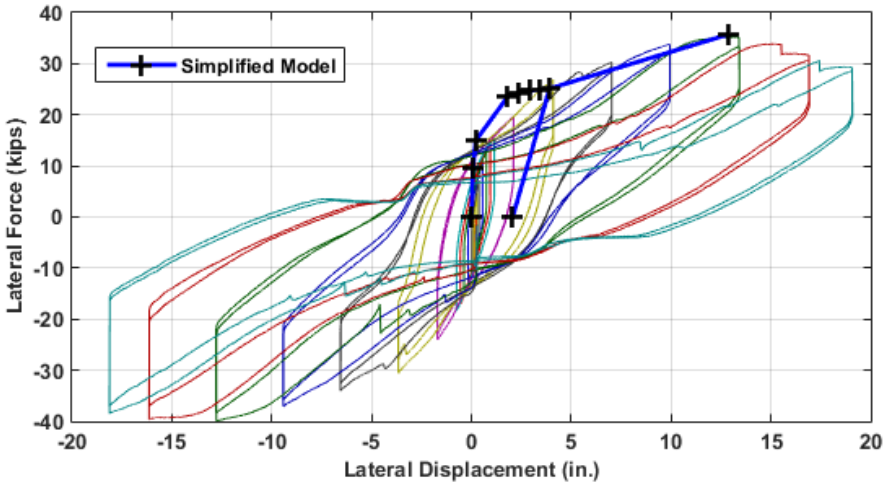

(a)

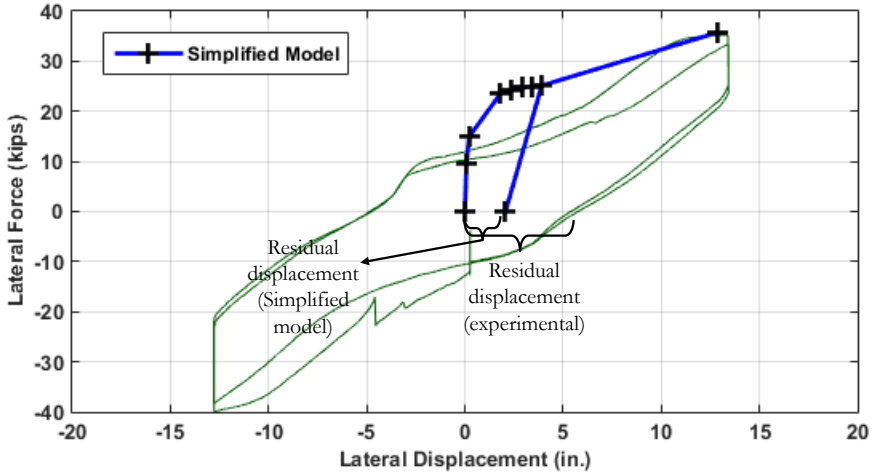

(b)

Figure 8: Comparison between the simplified model and experimental results, (a): complete cycle, (b): last cycle.

2.3. Detailed Analytical models

In this section, a more general and detailed analytical model is presented. In the previous simplified model, only key stages of the column deformation were considered, while consideration of different sets of equations at different stages was found to lack robustness under random selection

of design/system variables. Also, the lack of the cyclic pushover capability did not allow predictions of hysteretic energy dissipation.

The new model is generalized and capable of predicting the response for any given lateral deformation through the same set of equations throughout the analysis, while it is also capable of conducting cyclic pushover analysis. The column area is divided into two sections, an interior section having a confined concrete material behavior and an exterior section having unconfined concrete section behavior. A typical cross-section discretization considered in the model is shown in figure below

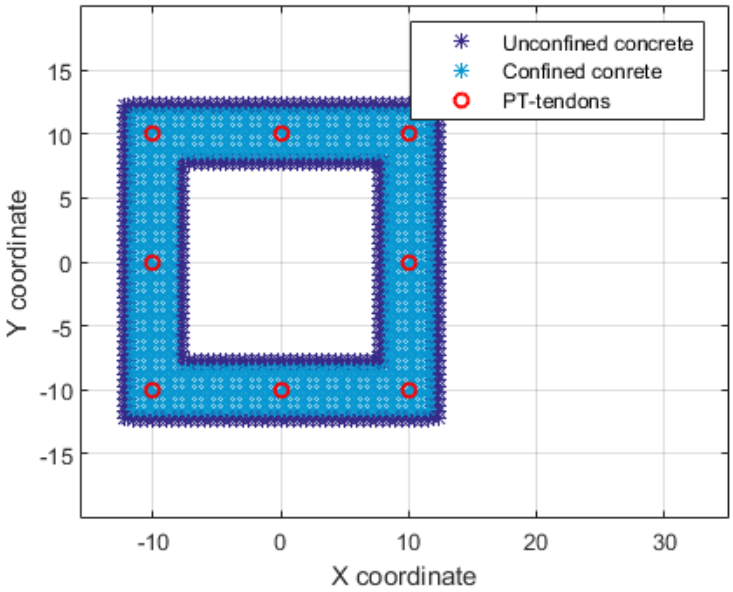

Figure 9: Cross-Section discretization for the detailed model.

Two types of detailed analytical model is discussed in this section. The first model considers curvature as the input parameter whereas the second model considers displacement as input parameter. The reason for transitioning from the first to the second model is that, in the presence of softening materials, the curvature does not always increase with the lateral displacement, making it an unsuitable control parameter for pushover analyses.

The second model, because it uses displacement as its input, can be used to conduct a dynamic analysis of HSR columns considering them as single degree of freedom systems. The detailed models are discussed further in the following subsections. Since this model is generalized for any state of deformation, some of the terms discussed in the previous model are revisited again. Lastly, a robust modified Newton-Raphson solver is adopted to solve the model.

2.3.1. Detailed Analytical Model – Model 1

In this section, a model that considers curvature ϕ as the control input parameter is formulated. The individual terms related to the compatibility and equilibrium condition is discussed. First, the equations related to computation of the concrete reaction force is discussed. Second, the equations for finding the forces in the PT tendons are discussed. Lastly, the set of equilibrium equations and the primary unknowns to be solved for is identified.

For a given curvature ϕ, and strain ε_0 at mid-section of the column show in Figure 10, the strain ε_c in a fiber located at a distance *x* from the mid-section is given as

$$\varepsilon_c = \varepsilon_0 + x\phi \tag{21}$$

Once the confinement properties of the concrete section are computed, the stress f_c in the concrete for any given value of strain ε_c can be computed from a compression-only hysteretic law bounded by the envelope curve from Mander et al. 1988:

$$f_c = \frac{f_{cc}\chi r}{r - 1 - \chi^r} \tag{22}$$

where χ is the ratio $\frac{\varepsilon_c}{\varepsilon_{cc}}$, with ε_{cc} being the strain at concrete confinement and f_{cc} being compressive strength of confined concrete. Also, *r* is given as:

$$r = \frac{E_c}{E_c - E_{sec}} \tag{23}$$

where E_c is the tangent modulus of elasticity of concrete and E_{sec} is given by the ratio $\frac{f_{cc}}{\varepsilon_{cc}}$. Using the above equations, the stress distribution along the column cross-section can be computed and hence the concrete reaction force N_c and moment M_c can be computed from integration.

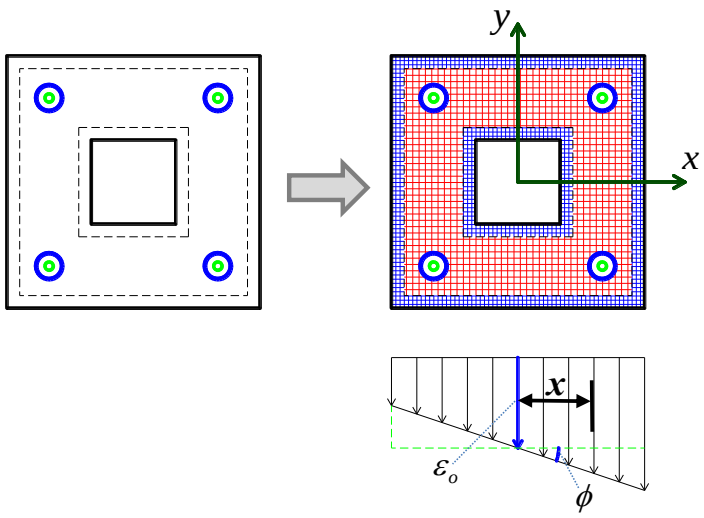

Figure 10: Variation of strain along the concrete cross-section

Based on the change in sign of concrete strain, the contact length c_r can be estimated as shown in Figure 11. The rocking rotation θ_r can be expressed as a function curvature and equivalent plastic hinge length l_r as given below

$$\theta_r = l_r \phi \tag{24}$$

where, the plastic hinge length l_r is estimated as a function of c_r using an equation originally proposed by (Roh 2007) and later modified by Sideris 2012:

$$\frac{l_r}{d} = a_r e^{-|r_c^3|} 0.5\sqrt{1 - r_c^2 + 2\sqrt{1 - r_c^2}} \begin{cases} r_c = \dfrac{c_r}{d} \\ a_r = 0.3 - 0.4 \end{cases} \tag{25}$$

Using the rocking rotation, the extension in PT-tendon due to rocking can be computed. The extension in PT-tendon due to rocking is given as:

$$u_{PT,i}^{(r)} = u_{PT,0}^{(r)} - x_{PT,i}\theta_r \tag{26}$$

Here, $x_{PT,i}$ is the distance of the PT tendon '*i*' from the mid-section and $u_{PT,0}^{(r)}$ is the extension in the tendon at the mid-section of the column shown in Figure 11:

$$u_{PT,0}^{(r)} = |\theta_r|\left(|x_{peak}| - c_r\right) \tag{27}$$

The total extension in the tendon is given as :

$$u_{pt,\mathrm{i}} = \underbrace{u_{PT,i}^{(0)}}_{\substack{\text{Due to}\\ \text{initial}\\ \text{PT}}} + \underbrace{u_{PT,i}^{(r)}}_{\substack{\text{Due to}\\ \text{rocking}\\ \text{at bottom}}} + \underbrace{\sum_{j=1}^{N_j} u_{PT,i,j}^{(sl)}}_{\substack{\text{Due to}\\ \text{joint sliding}}} \tag{28}$$

In above equation, the term $u_{PT,i}^{(0)}$ is the extension in the tendon due to initial Post-tensioning and $\sum_{j=1}^{N_j} u_{PT,i,j}^{(sl)}$ corresponds to the extension in the tendon due to sliding across all the joints and is given as

$$u_{PT,i,j}^{(sl)} = \left[2h_{da}\left(\frac{1}{\cos\left(\psi_j\right)} - 1\right)\right] \tag{29}$$

Here ψ_j is the tendon deviation angle due to sliding at the *j*-th joint and is defined in equation (9). In this model, it is assumed that the current sliding $u_{sl,j}$ is the same at all joints. This assumption is made in order to simplify the complexity of the model.

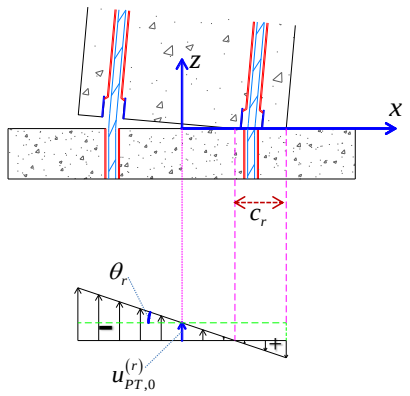

Figure 11: Relation between concrete compressive strain and contact length

Once the total extension in the tendons are computed, the strain in the tendons can be easily computed. The response of the tendons was obtained by a tension-only stress vs. strain hysteretic law by Sideris et al. 2014a bounded by the envelop curve from (Mattock 1979) given as:

$$\sigma_{PT} = E_{PT}\varepsilon_{PT}\left\{r_{PT} + \left(1 - r_{PT}\right)\left[1 + \left(\frac{E_{PT}\varepsilon_{PT}}{Kf_{Py}}\right)^{R}\right]^{-1/R}\right\} \quad \textbf{(30)}$$

where σ_{PT} is the axial tensile stress of the PT tendon, ε_{PT} is the tensile strain of the PT tendon, r_{PT} is the ratio of post-elastic to elastic modulus of the PT tendon, K is the ratio of actual yield stress to nominal specified yield stress (usually slightly larger than 1), and R is a dimensionless factor that determines the smoothness in transition from elastic to inelastic range. A typical stress strain curve obtained from Mattock model with important features are given in Figure 12. The behavior of the concrete model and the PT tendon model subjected to loading and unloading is given in Figure (14).

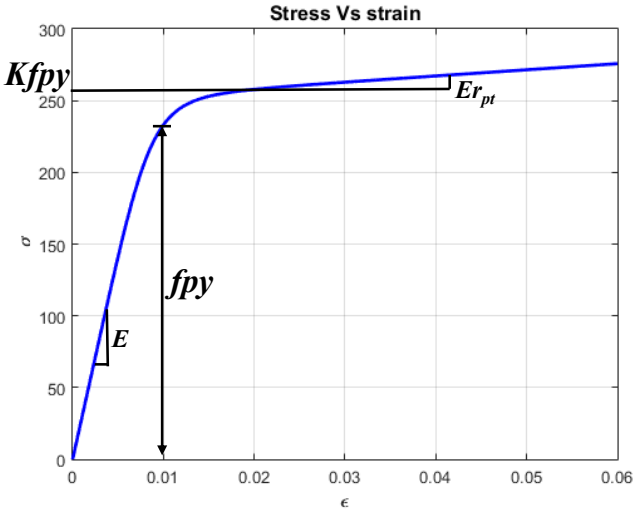

Figure 12: Typical Mattock model with key features.

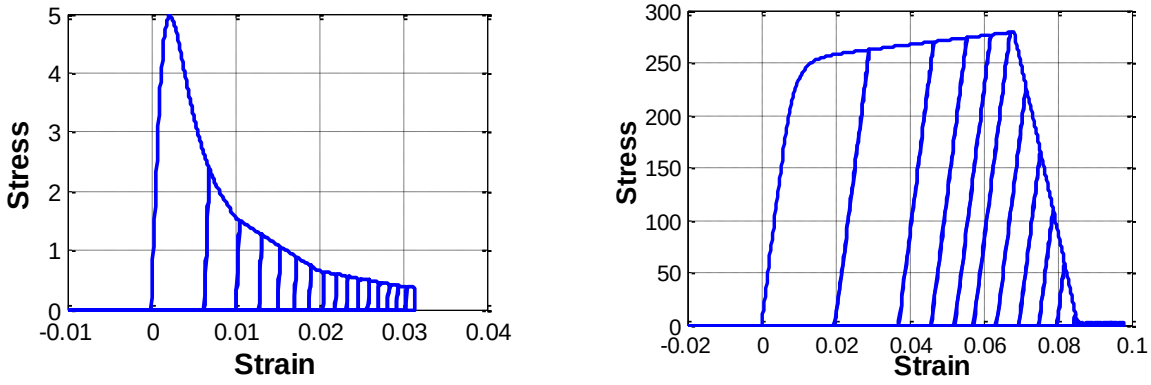

(a) **(b)**

Figure 13 : (a) Typical cyclic behavior of concrete model, (b) Cyclic behavior of PT tendons.

Once the stresses in the tendons are computed, the total PT force (N_{pt}) can also be calculated. The terms N_{PT} and N_c for any given state of damage can be computed using the set of equations discussed in this section. However, the values of N_c and N_{PT} computed should also satisfy the equilibrium and compatibility conditions. The equations for vertical and moment equilibrium presented in the simplified model are generalized enough to be used for any state of damage. However, the equilibrium equations relating the horizontal force and joint-shear force of a SD joint

are applicable only for the unloading stages. In the improved model, a more generalized relation for joint shear equilibrium applicable for any state of damage is used.

At the SD joints, the applied horizontal force is resisted by the joint shear force given as (Sideris et al 2014):

$$V_j = \left(\underbrace{\mu_j \left(N_c \right) Z\left(u_{sl,j} \right)}_{Friction\ Force, V_{R,f}^j} + \underbrace{N_{PT,tot} \sin\left(\psi_j \right)}_{Bearing\ Force, V_{R,b}^j} + \underbrace{K_l \left\langle \left| u_{sl,j} \right| - u_{sl,l} \right\rangle \mathrm{sgn}\left(u_{sl,j} \right)}_{Locking, Force, V_{R,L}^j} \right) \quad \textbf{(31)}$$

The first term is the above equation is the shear resistance at the joint due to friction force. The term $Z\left(u_{sl,j} \right)$ is an elasto-plastic hysteretic function (Z = ±1 at sliding initiation) to capture the effects of sliding. The variation of *Z* with sliding displacement is shown in Figure 14. The second term is the shear resistance due to tendon bearing force, which is initiated once tendons are in contact with the ducts. Due to the dowel effect of the PT tendon, the bearing forces are activated. The third term is the locking force, which are the stiffening forces that initiate once the sliding capacity ($u_{sl,l}$) is reached and the tendons are in contact with the bottom and top duct adaptor. The above three terms are visualized in Figure 15 (Sideris et al. 2014c) and the typical variation of the joint shear force with joint sliding is show in Figure 16. In the next subsection, the detailed model is formulated highlighting important equations and the primary unknowns to be solved for are defined.

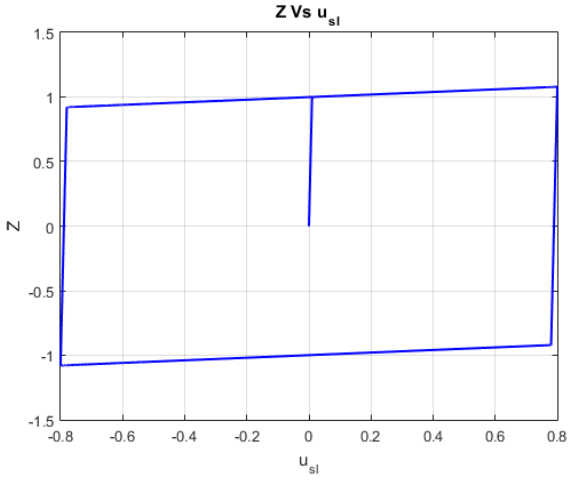

Figure 14: Variation of Z with sliding displacement u_{sl}.

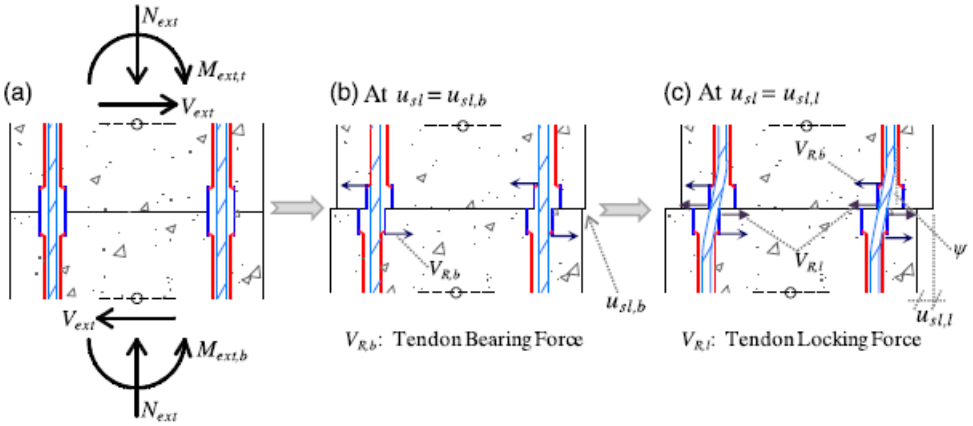

Figure 15: Response of SD joint showing Tendon bearing and locking forces. (Sideris et al. 2014c)

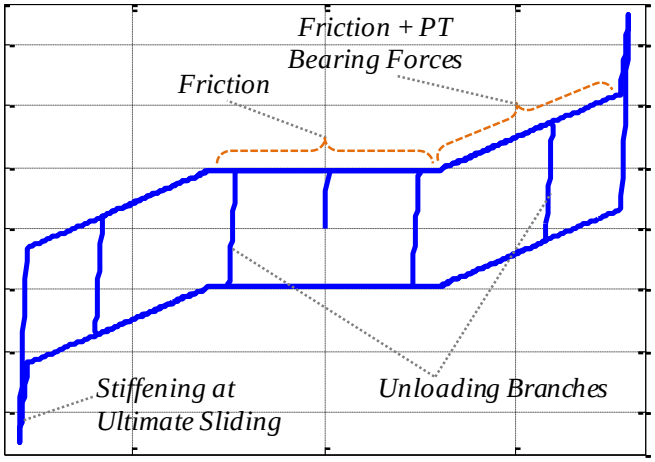

Figure 16: Variation of joint-shear force V_j with joint sliding u_{sl}.(Sideris et al. 2014c)

2.3.1.1. Model formulation and computational implementation

In this section, the equilibrium equations to be solved, primary unknowns and the solution procedure are discussed. The input variable that determines the state of deformation in the system is ϕ, while the primary unknown are ε_0 and u_{sl}. The equilibrium equations to be solved are

$$\{f\} = \begin{Bmatrix} f_1 \\ f_2 \end{Bmatrix} = \begin{Bmatrix} P_v + N_{PT,tot} - N_c \\ P_h - V_j \end{Bmatrix} \quad \textbf{(32)}$$

For a given value of ϕ, the individual terms in the above set of simultaneous nonlinear equations are computed and solved for ε_0 and u_{sl}. A Newton-Raphson algorithm is used to solve the above set of equations. The Newton-Raphson method is an iterative procedure where the unknown variables are estimated in each iteration using the derivatives of the equation. This procedure can be written in form of equation as

$$\{x_{i+1}\} = \{x_i\} - [J]^{-1}\{f\} \quad \textbf{(33)}$$

where, $\{x_i\}$ is the guess of ε_0 and u_{sl} in the iteration step *i*, and $[J]$ is the Jacobean of the function $\{f\}$ defined as:

$$[J] = \begin{bmatrix} \dfrac{df_1}{d\varepsilon_0} & \dfrac{df_1}{du_{sl}} \\ \dfrac{df_2}{d\varepsilon_0} & \dfrac{df_2}{du_{sl}} \end{bmatrix} \quad \textbf{(34)}$$

Here, the entries of the Jacobean matrix are the partial derivatives of $\{f\}$ with respect to ε_0 and u_{sl}. Once the right solution for to ε_0 and u_{sl} is found, the horizontal displacement is then computed using the equation (13). Since the model is highly nonlinear, a robust Newton-Raphson solver was very important. In this solver, whenever the algorithm fails to find a solution within a given number of iterations, the target ϕ is scaled down. In this way, the algorithm solves with more points of

input ϕ the sections of the pushover curve that do not have smooth transitions. This situation mainly occurs during sliding initialization stage of the pushover curve. The model proposed in this section is generalized enough to be applicable for cyclic pushover analysis.

A typical cyclic pushover curve from the detailed model is shown in Figure 17 below. Since the pushover curve consists of many states of stress, the resultant pushover curve much smoother than the previous model. Further it can be noticed that the sliding behavior of the column and unloading stages are captured well in this model.

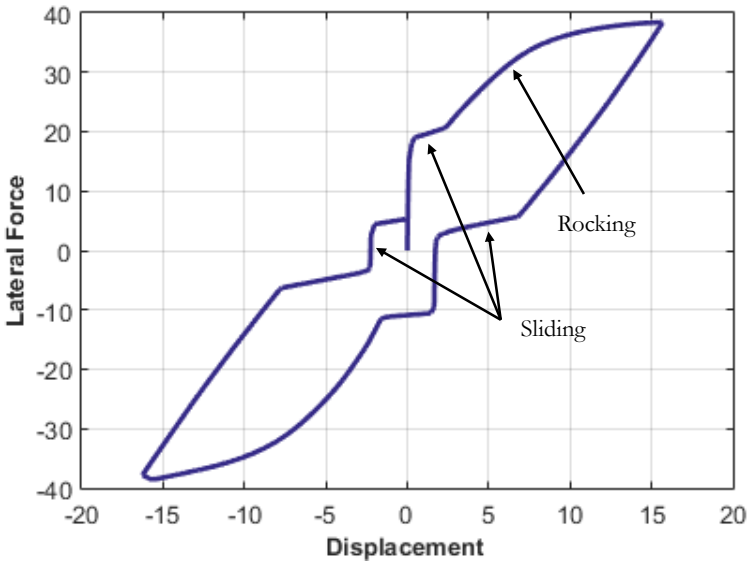

Figure 17: Typical pushover curve from detailed model.

*2.3.2. Detailed Analytical model - **Model 2***

The motivation for the development of the second analytical model is: (i) in the presence of softening materials (e.g., concrete), the curvature does not always increase monotonically with the lateral displacement, making it an unsuitable control parameter for pushover analyses, (ii) for implementation within a structural analysis framework or software (as a simplified nonlinear spring), a model that provides column lateral force for given lateral displacement is typically required. For this reason, the second model uses lateral column displacement as the input/control

parameter. Most of the equilibrium and compatibility equations are similar to the previous model. However, some of the terms and equations had to be reformulated. The model is graphically shown in Figure 18. The model includes a constant strain/curvature plastic/rocking hinge at the bottom, in series with an elastic column member and a rigid element to connect the top of the column with the center of mass of the superstructure.

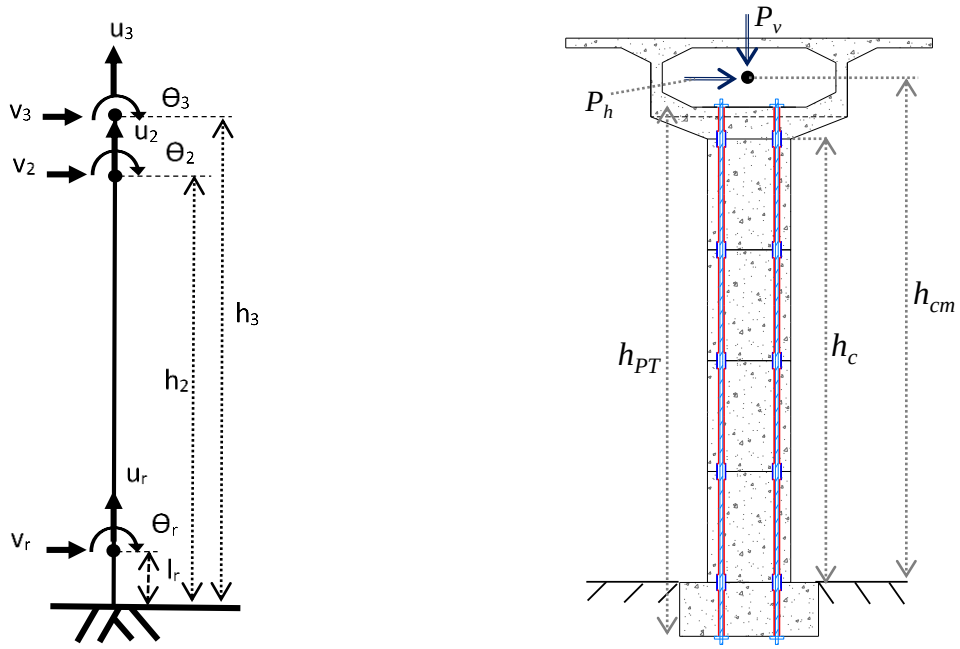

Figure 18: Free body diagram showing the displacements and forces in HSR column.

2.3.2.1. Equivalent Plastic hinge length

In this model, the equivalent plastic hinge length (due to rocking) is considered to be a constant fraction of the cross-section depth (0.8~0.9d). This approximation makes the estimation of rocking angle simpler (and more robust) and was found to have small influence on the predicted response.

2.3.2.2. Kinematics and strain-displacement equations.

The **Error! Reference source not found.** given below is the free body diagram of the HSR column. The extension in the tendon due to rocking is given as:

$$u_r = -l_r \varepsilon_0 \quad \textbf{(35)}$$

Rotation due to plastic deformation is given as $\theta_r = l_r \phi$ **(36)**

The displacement due to resultant plastic deformation is given as

$$v_r = \frac{1}{2} l_r \theta_r \quad \textbf{(37)}$$

The relation used for relating horizontal displacement and horizontal force is given as

$$v_3 \, or \, u_h = v_2 + \theta_2 \left(h_3 - h_2 \right) \quad \textbf{(38)}$$

where

$$\theta_2 = \frac{P_h}{2EI} \left(h_2 - l_r \right)^2 + \frac{P_h}{EI} \left(h_3 - h_2 \right) \left(h_2 - l_r \right) + \theta_r \quad \textbf{(39)}$$

and

$$v_2 = \frac{P_h}{3EI} \left(h_2 - l_r \right)^3 + \frac{P_h}{2EI} \left(h_3 - h_2 \right) \left(h_2 - l_r \right)^2 + \left(h_2 - \frac{l_r}{2} \right) \theta_r \quad \textbf{(40)}$$

The extension in the column due to rocking at mid-section is now given as

$$u_3 = u_2 = u_r - \left(N_c \right) \frac{\left(h_2 - l_r \right)}{AE} \quad \textbf{(41)}$$

2.3.2.3. Moment equilibrium equation

The moment equilibrium condition in previous models considers the secondary effects of the column sliding. In this model, the secondary effect due column displacement is considered instead and is given by equation:

$$P_h = \frac{M_c + M_{PT,tot} - P_v u_h}{h_m} \quad \textbf{(42)}$$

2.3.2.4. Formulation of the model and computational implementation

In this model, the parameter that determines the damage of the column is horizontal displacement u_h. The primary unknowns in this model are ε_0, ϕ, u_{sl} and P_h The equilibrium equations to be solved in the Newton-Raphson solver are:

$$\begin{Bmatrix} f_1 \\ f_2 \\ f_3 \\ f_4 \end{Bmatrix} = \begin{Bmatrix} P_v + N_{PT,tot} - N_c \\ P_h - \left(\mu_j \left(P_v + N_{PT,tot} \cos\left(\psi_j\right) \right) Z\left(u_{sl,j}\right) + N_{PT,tot} \sin\left(\psi_j\right) + K_l \left\langle \left| u_{sl,j} \right| - u_{sl,l} \right\rangle \operatorname{sgn}\left(u_{sl,j}\right) \right) \\ v_3 - u_h \\ \dfrac{M_c + M_{PT,tot} - P_v u_h}{h_m} - P_h \end{Bmatrix} \quad \textbf{(43)}$$

It is noted that in the last equation large deformation effects have been considered using in entire lateral deformation, rather than the effect of joint sliding only.

The Jacobian to be used for solving the above equation are:

$$\left[J\right] = \begin{bmatrix} \dfrac{df_1}{d\varepsilon_0} & \dfrac{df_1}{d\phi} & \dfrac{df_1}{du_{sl}} & \dfrac{df_1}{dP_h} \\ \dfrac{df_2}{d\varepsilon_0} & \dfrac{df_2}{d\phi} & \dfrac{df_2}{du_{sl}} & \dfrac{df_2}{dP_h} \\ \dfrac{df_3}{d\varepsilon_0} & \dfrac{df_3}{d\phi} & \dfrac{df_3}{du_{sl}} & \dfrac{df_3}{dP_h} \\ \dfrac{df_4}{d\varepsilon_0} & \dfrac{df_4}{d\phi} & \dfrac{df_4}{du_{sl}} & \dfrac{df_4}{dP_h} \end{bmatrix} \quad \textbf{(44)}$$

The material models and procedure used to find the solution are similar to the previous model. The figure given below is the plot of cyclic pushover curve. It can be noticed that the pushover curve obtained from both the models are very similar. However, the peak forces for the model-2 are lesser because of the fact that secondary effect due to total displacement is considered in model-2.

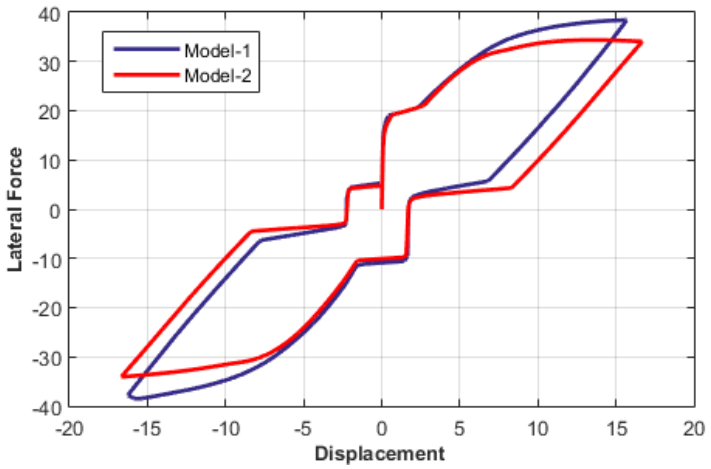

Figure 19: Comparison in pushover curves obtained from model-1 and model-2

2.4. Validation of the models

In this section, both the proposed model-2 is compared with the results of quasi-static cyclic testing described in section 2.2.5. Figure 20 given below shows the results from the detailed model 2 and the experimental results. Since we can input the displacement pattern similar to the experiment (continuous cyclic pushover with increasing amplitude) in the detailed model, it can be seen that the results from this model is much better than that of the simplified model. The peak horizontal force and displacements are predicted better when compared with the previous model. However, the residual displacements are still underestimated by about 70%. Since the overall cyclic behavior of the model is captured fairly well by this model, it can be used to estimate the hysteretic damping of HSR columns. The variation of joint shear with sliding displacement at each joint is also compared in Figure 21. Since the model assumes same sliding displacements in all the joints. The estimates for joint sliding match well only with some joints. However, the estimation of peak joint shear force is predicted well for most of the joints. In the next section, various design variables are examined and their effect on the behavior of the column are discussed.

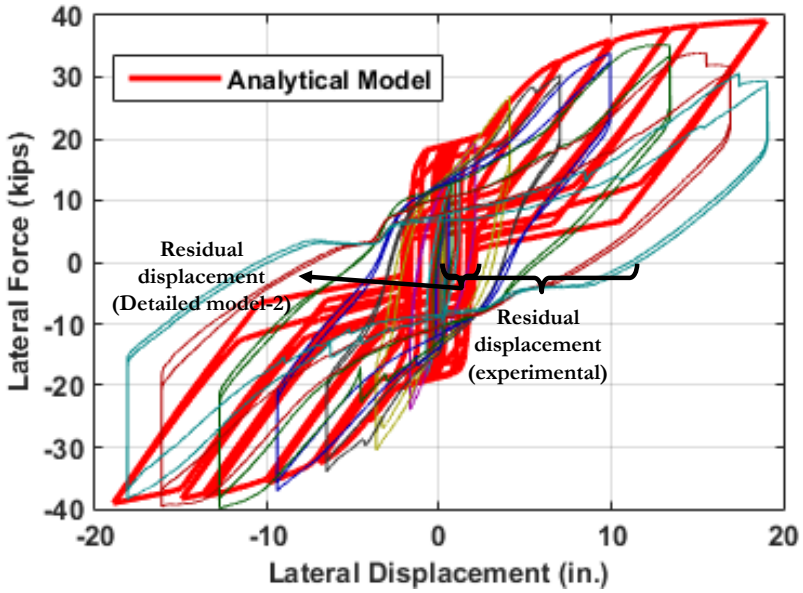

Figure 20: Comparison of experimental result with detailed model.

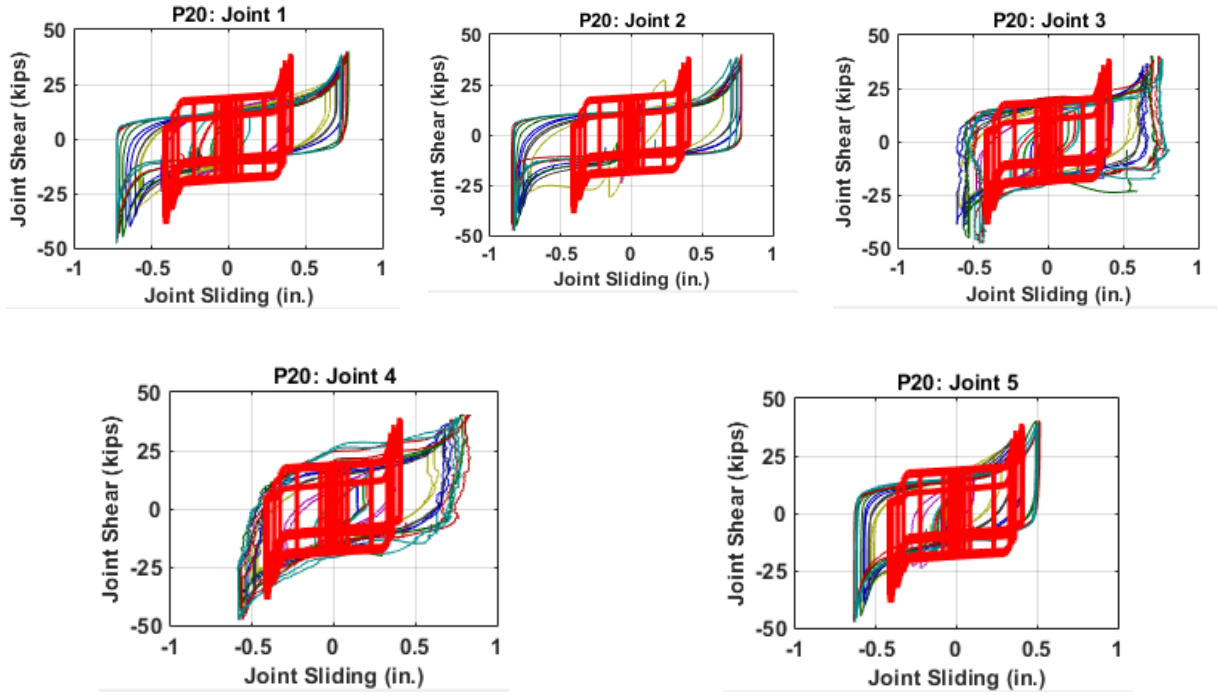

Figure 21: Joint shear force Vs joint sliding at each joint.

2.5. Assessment of Design variables

In this section, a single cycle pushover analysis is conducted by varying major design parameters – one at a time – of the HSR parameters. This assessment provides a better idea on how some of

the design parameters affect the performance of HSR columns. The effect of coefficient of friction (COF) at the SD joints is investigated first. From Figure 22(a) it is observed that the response of a HSR columns with high COF is similar to response of rocking-only columns. Increasing the COF increases the forces in tendon causing them to break. Therefore it can be noticed that allowing the column to slide provides a more ductile response. Figure 22(b) shows the effect of COF on joint shear force and joint sliding. Having high COF delays initiation of sliding, which also occurs at a larger shear force, and reduces the peak sliding.

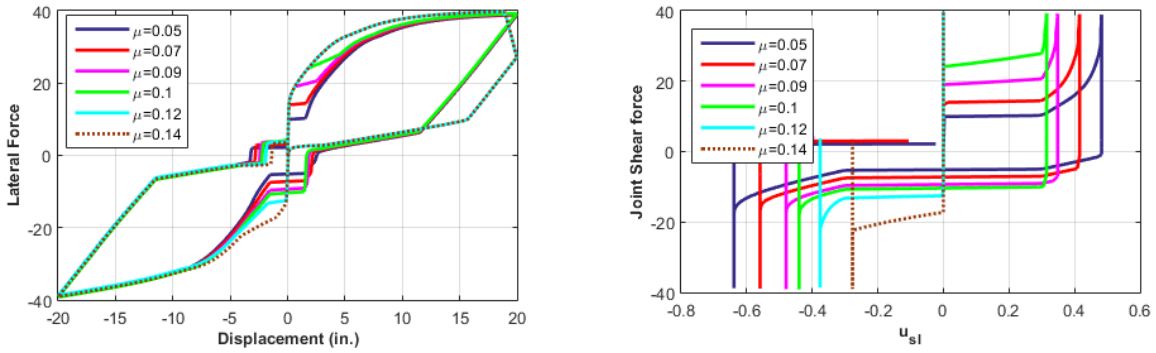

(a) **(b)**

Figure 22: Effect of COF on (a) Pushover, (b) Joint shear-force and sliding.

Next, the effect of diameter of duct adaptor is examined. In Figure 23, it is observed that reduction in duct diameter reduces the peak sliding capacity. This causes the initiation of tendon bearing and locking forces earlier when compared to higher duct diameters. This leads to failure of tendons. This parametric study shows that the performance of the HSR column is greatly affected by the choice of design parameters. Efficient designs can be achieved with the right choice of these parameters.

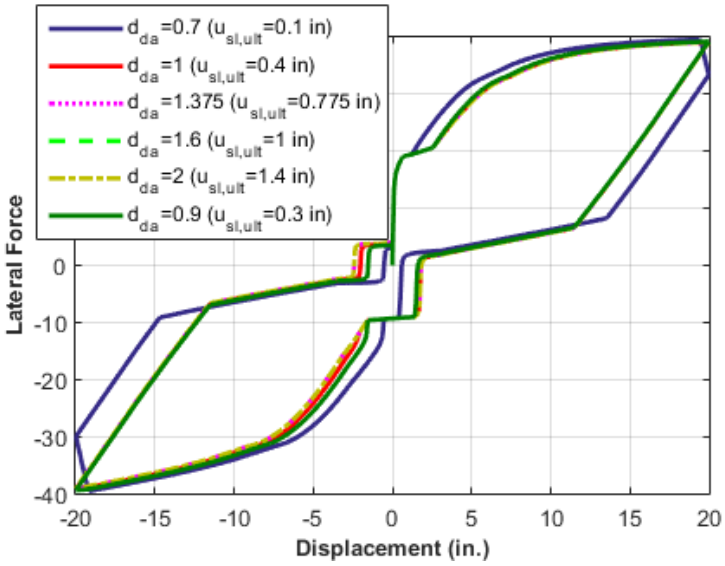

(a)

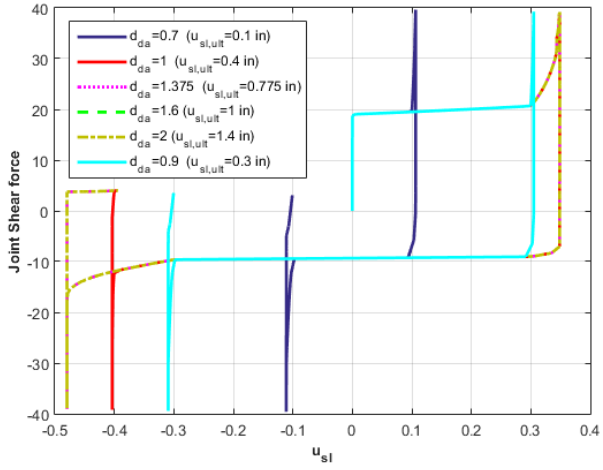

(b)

Figure 23: Effect of diameter of duct adaptor on (a) Pushover, (b) Joint shear-force and sliding.

Next, the effect of the vertical force P_v and initial force of PT tendon is examined. Figure 24 given below shows the effect of vertical force and initial PT on Pushover curve. It can be noticed that increasing the vertical force and PT force increases the horizontal force. However, it can be noticed that the effect of increase in lateral force due to increase in PT tendon is much higher when compared with the horizontal forces. This clearly shows that there is a significant contribution to

the pushover curve from the PT tendons. From the above parametric study it can be noticed that, the diameter of the duct adaptors, coefficient of friction and initial PT force are some of the important design parameters. These parameters must be chosen appropriately for optimal designs.

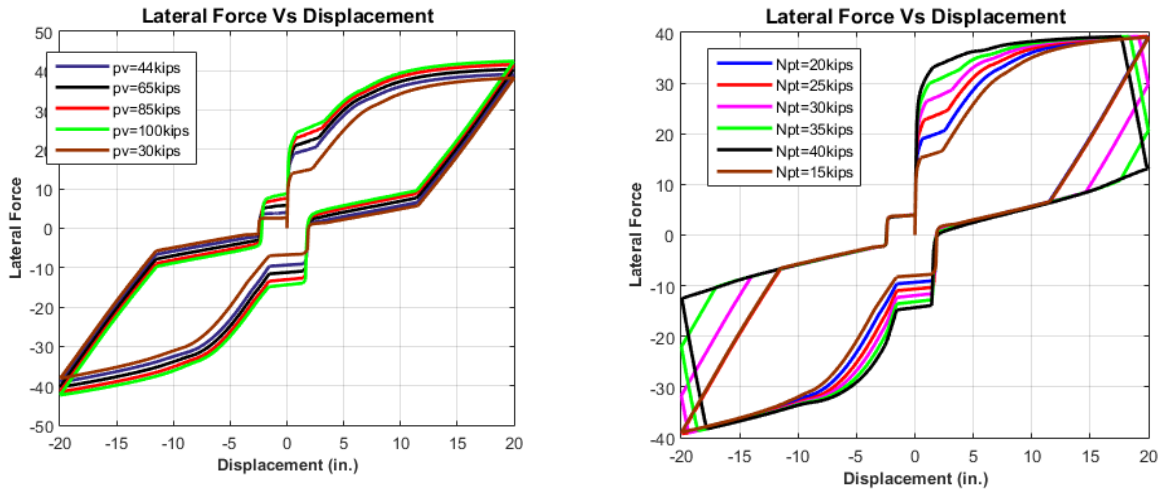

(a) (b)

Figure 24: Effect of Vertical force (a) and Initial PT force (b) on Pushover curve.

2.6. Major findings

In this chapter, a simplified model to estimate the pushover curve of HSR column was derived. The simplified model was compared with experimental results. It was observed that peak horizontal forces were estimated well but the unloading section of pushover did not match well. In order to have a more generalized pushover curve capable of conducting cyclic pushover analysis, detailed models were developed. Two detailed models were developed, one with curvature as input and one with horizontal displacement as input. Both the detailed models use concrete and PT tendon hysteretic material models that match well with experimental results. The detailed models were then compared with experimental results. It was observed that the detailed models perform much better than the previous model. The cyclic behavior of HSR columns are predicted well in the detailed model. Lastly, a small parametric study is conducted to examine the

effects of various design parameters. In the next section, the detailed model is used in a Capacity spectrum design framework to propose a design methodology for HSR columns.

3. CAPACITY SPECTRUM DESIGN METHODOLOGY FOR HSR COLUMNS

In this section, a capacity spectrum design methodology is presented for the HSR columns. In the first sub-section, the design procedure for HSR columns is discussed. The design procedure is applied for a typical column to estimates the performance point of the column for given level of hazard. In the second sub-section, a nonlinear dynamic analysis is conducted on the typical column to verify the results of design methodology.

3.1. Design methodology

A general flow chart of the capacity spectrum method shown in the flowchart given below in Figure 25.

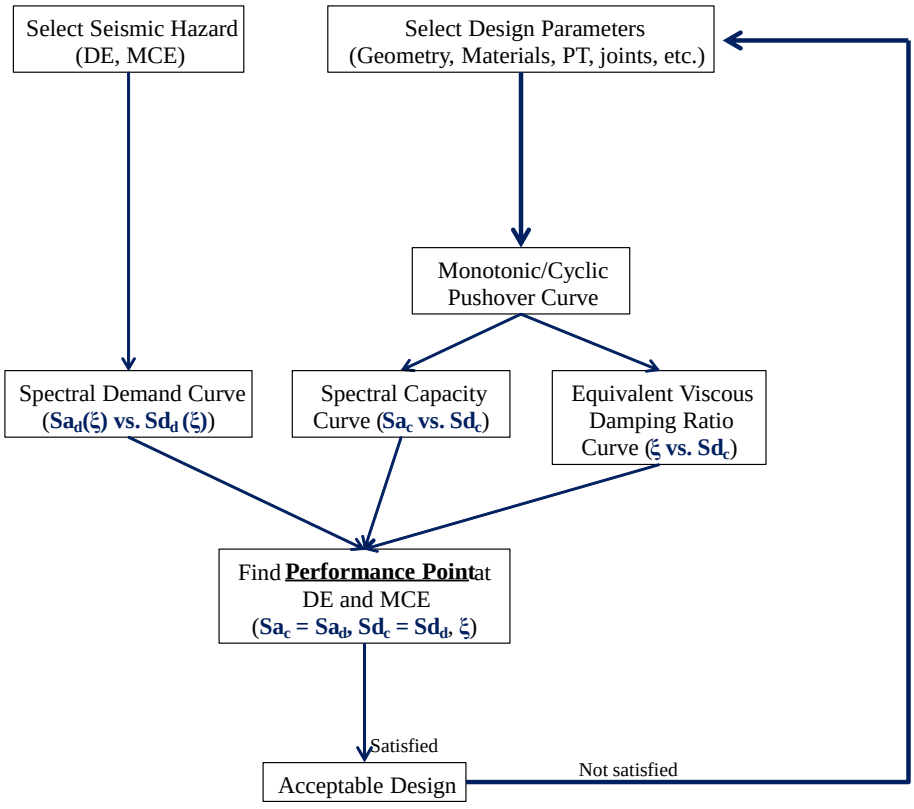

Figure 25: Capacity Spectrum Method Flow-Chart

In capacity spectrum design, the nonlinear pushover curve is converted to the so-*called spectral capacity curve*, which is a spectral acceleration vs. spectral displacement curve (Discussed in section 3.1.2) . Next a *seismic demand curve* from typical design response spectra is scaled to account for hysteretic damping affects (Discussed in section 3.1.1). The point of intersection of the spectral capacity curve with the spectral demand curve is termed the *performance point*. This indicates the performance of the system when it is subjected to a hazard represented by the demand curve. If there is not a point of intersection, this means that the system will fail at the given hazard. In order to incorporate capacity spectrum design, the nonlinear pushover curve of the structure is required. This procedure also requires the estimation of variation of equivalent viscous damping with lateral displacement (and spectral displacement). In this section, a capacity spectrum design methodology is proposed for HSR columns. In the first subsection, procedure to obtain the seismic demand curve is explained. Next the seismic capacity curve is estimated. Finally the numerical procedure to find the performance point is presented.

3.1.1. Seismic demand

In performance based seismic design, establishment of seismic demand is an important step. Two levels of seismic hazard are considered in this study. The first is the Design earthquake (DE, 10% probability of exceedance in 50 years), and the Maximum considered earthquake (MCE, 2% probability of exceedance in 50 years). The response spectra for any given level of hazard is computed per AASHTO LRFD Bridge design Specifications 2007:

$$S_A = \begin{cases} 2.5A, & T \le 0.33S^{\frac{3}{2}} \\ \dfrac{1.2AS}{T^{\frac{2}{3}}}, & 0.33S^{\frac{3}{2}} < T < 4 \\ \dfrac{3AS}{T^{\frac{4}{3}}}, & T \ge 4 \end{cases} \quad \textbf{(45)}$$

This spectrum refers to the seismic event with 10% in 50 years probability of exceedance and soil profile type I and II. The acceleration coefficient is obtained from seismic hazard map and S is the site coefficient which represents the soil profile type. To scale the response spectra for any given value of damping, equation (46) (European Committee for Standardization 1994) is used. Here, ξ_{eq} is the equivalent damping in the system. In this study, the bridge under study was assumed to be located at a moderate to high seismicity area in California with A=0.25, with a soil profile of type II (S=1.2 per table 3.10.5.2) of AASHTO LRFD Bridge design Specifications 2007.

$$S_{A,\xi_{eq}} = \sqrt{\frac{0.07}{0.02 + \xi_{eq}}} S_A \quad \textbf{(46)}$$

3.1.2. Seismic capacity

The seismic capacity for the capacity spectrum method is computed by conducting a monotonic pushover analysis on the structure. The resultant force versus displacement curve is then expresses as spectral acceleration vs. spectral displacement curve, which for a single degree of freedom system is given by:

$$S_{A,c} = \frac{P}{m} \quad and \quad S_{D,c} = u \quad \textbf{(47)}$$

where, *P* is the horizontal load obtained from pushover curve, *m* is the mass of the structure and *u* is horizontal displacement of the structure.

3.1.3. Damping curve

Damping ratio for a system for any given displacement u can be estimated using the cyclic pushover curve is given as.

$$\xi(u) = \xi_o + \xi_{hyst}(u) \tag{48}$$

where ξ_o is the inherent damping in the system (~ 3-5%), and $\xi_{hyst}(u)$ is the damping ratio due to hysteresis obtained as:

$$\xi_{hyst}(u) = \frac{1}{4\pi}\frac{E_{hyst}(u)}{E_s(u)} \tag{49}$$

where $E_{hyst}(u)$ is the energy dissipated due to hysteresis, and $E_s(u)$ is the elastic energy that equivalent elastic secant stiffness system. The energy dissipated and stored are shown in Figure 26 (a) given below. For each point in the curve, a cyclic pushover curve is conducted to get a smooth variation of damping ratio with displacement.

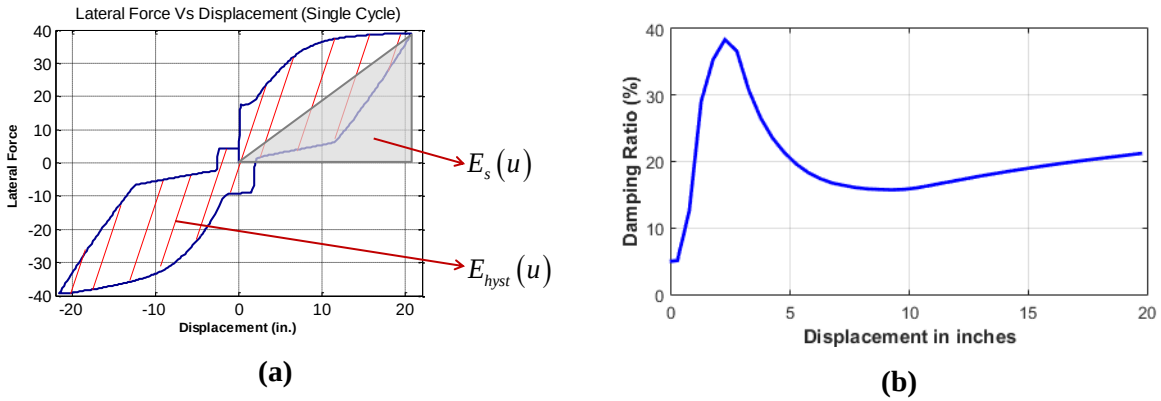

(a) **(b)**

Figure 26: (a) Energy stored and dissipated in a typical hysteretic curve, (b) Variation of Damping curve with displacement.

3.1.4. Performance point

As mentioned earlier, the displacement at which the capacity curve meets the demand curve is called the performance point. The demand curve at a given spectral displacement is scaled due to

the damping ratio at that displacement given by the damping curve (Figure 26 (b)). Therefore, in order to find the performance point, this scaling should be taken into account. The mathematical problem can be stated as: $H(SD) = SA_c(SD) - SA_d\left((SD), \xi\left((SD)\right)\right)$, where SD is the spectra displacement that is equal to the lateral column displacement for a single degree of freedom system. To find the performance point, the demand, capacity and damping curves are first computed. Then, a bi-section method is formulated as:

i. Start with a small and large initial guess of spectral displacement at the performance point.
ii. Find the damping ratio corresponding to both spectral displacements
iii. Find the value of the spectral demand at that spectral displacements corresponding to the computed damping ratios
iv. Find the value of the spectral demand at that spectral displacements
v. Find the displacement where capacity curve meets the demand curve
vi. Select a new initial guess as the average of the two spectral displacements and check if $|H(SD)| < tolerance$. If not, repeat the process from step ii in accordance with the Bi-section method, until convergence is achieved

Computationally, a bisection algorithm was used find the performance.

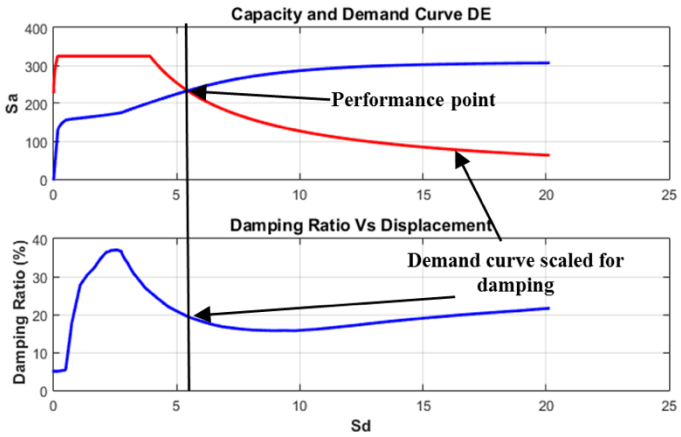

Figure 27: Plot showing capacity vs. demand curve and damping vs. displacement.

3.2. Validation of proposed methodology using Incremental Dynamic Analysis (IDA)

In this section, the performance points obtained from the proposed capacity spectrum design methodology is verified using the results of nonlinear dynamic analysis on the structure. To conduct nonlinear dynamic analysis, the HSR column is considered as a single degree of freedom system (SDOF). This SDOF is subjected to a set of ground motions and analyzed to find the peak displacement of the structure. The applied ground motions (GM) are then scaled until the structure fails. This procedure is called incremental dynamic analysis (IDA). A plot of a peak response parameter for a given GM vs. intensity measure (usually the spectral acceleration) is called an IDA curve. The peak response corresponding to the scale that is representative of the hazard is the actual performance of the structure for the given hazard. In the following subsections, the incremental dynamic analysis is further explained in detail.

3.2.1. Dynamic analysis of HSR column as SDOF system

The HSR columns can be simplified as a SDOF system with a lumped mass acting at the top of the column. The force displacement relation for the SDOF system is obtained from the detailed

analytical model proposed in section 2.3.2. The solution for the dynamic analysis is for ground excitation is computed numerically using Newmark's beta method.

3.2.2. Ground motion records

For the dynamic analysis of HSR columns all the records of (FEMA) 2009 Far-field ground motion set was considered in this study. For the ground motions to represent the seismic demand curve, the scale factor corresponding to the ground motions are estimated. Three different methods were followed in this study

- Method-1: According to ASCE 2010, the mean spectrum of ground motions must envelop the design spectrum between $0.2T_n$ and 1.5 T_n, where T_n is the elastic fundamental period of the system.
- Method-2: Mean spectrum of ground motions enveloping the design spectrum at T_{sec}, where T_{sec} is the secant period of the structure at the performance point predicted by the proposed CSM. This must give a better estimate of demand curve, as the spectrum accounts for the damage in the structure at performance point.
- Method-3: Mean spectrum of ground motions enveloping the design spectrum at the elastic period T_n. Results corresponding to this scale would have the most discrepancy as it corresponds to the undamaged state of the structure.

  The design spectrum and the Mean spectrum of ground motions scaled using the above three methods are shown in Figure 28.

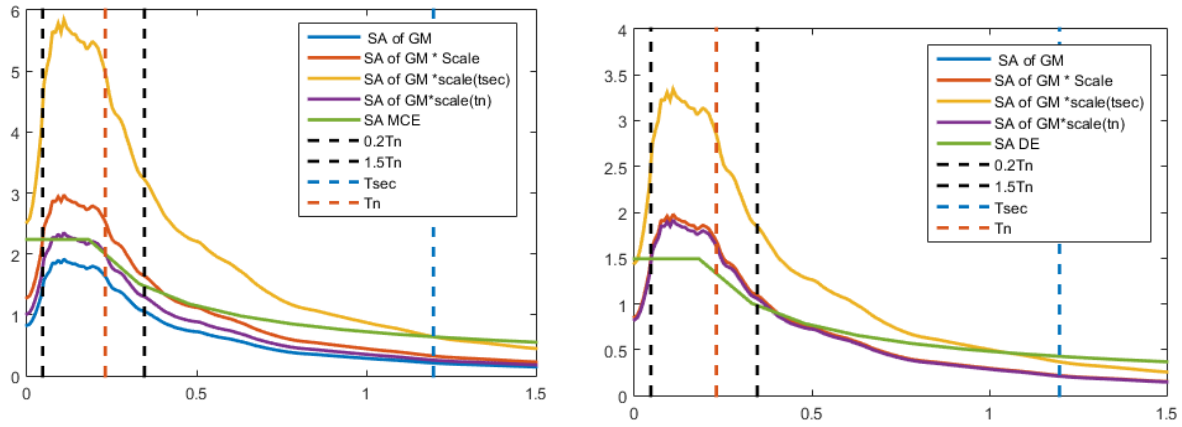

(a) **(b)**

Figure 28: Scaling of ground motion ensemble to represent demand curve (a: MCE, b: DE).

3.2.3. Incremental dynamic analysis

To develop IDA curves, the structure is analyzed for each ground motion for increasing scale factors until failure. A plot of mean of peak displacement of the structure (at a given scale factor) versus the intensity measure (can be scale factor or spectral acceleration at natural frequency T_n)is a mean IDA curve. From the mean IDA curve, the performance of the structure for a hazard is then obtained..

3.2.4. Comparison of results

Figure 29 shows the IDA curve for the structure. The plot shows the peak displacement for ground motion versus the spectral acceleration (intensity measure) at T_n, where T_n is the natural frequency of the column. The plot also shows the mean and the geometric mean of these results. For a given level of hazard, the scale factors are computed using the three methods discussed in previous section. The peak displacements for each ground motion pertaining to the computed scale factor is obtained from Figure 29. The mean and geometric mean of these displacements are then compared with the performance point obtained from capacity spectrum method.

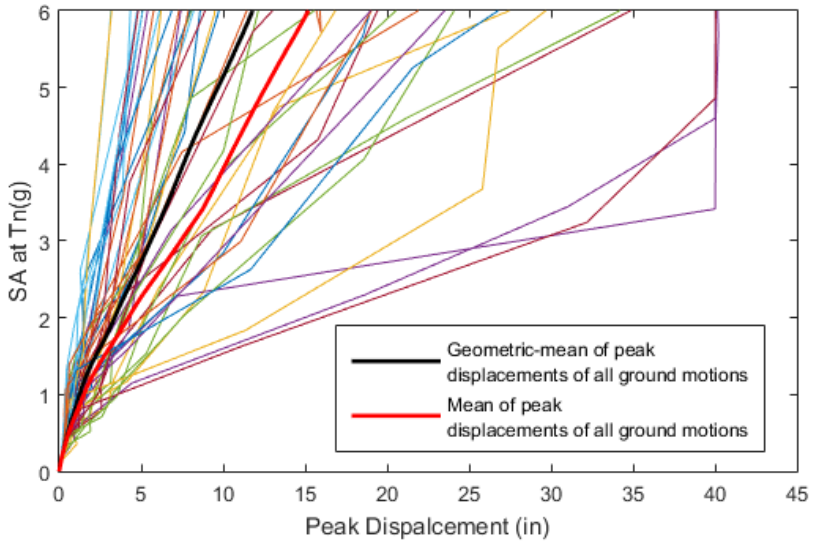

Figure 29: IDA curve showing Peak displacements versus Sa(T_n) for all the ground motions and mean peak displacements.

For the column dimensions and materials properties discussed in section 2.2.5, the performance points for DE and MCE, and comparison with IDA results are summarized below:

- **Performance point at DE (from CSM)** : **5.61 in**
    - Geometric mean peak displacement from Method 1: **2.47 in**
    - Mean peak displacement from Method 1: **2.71 in**
    - Geometric mean peak displacement from Method 2: **4.81 in**
    - Mean peak displacement from Method 2: **5.22 in**
    - Geometric mean peak displacement from Method 3: **2.32 in**
    - Mean peak displacement from Method 3: **2.59 in**
- **Performance point at MCE (from CSM)** : **7.56 in**
    - Geometric mean peak displacement from Method 1: **4.21 in**

- Mean peak displacement from Method 1: **4.53 in**
- Geometric mean peak displacement from Method 2: **9.69 in**
- Mean peak displacement from Method 2: **11.08 in**
- Geometric mean peak displacement from Method 3: **3.18 in**
- Mean peak displacement from Method 3: **3.38 in**

It can be noticed that the estimates obtained from the capacity spectrum method corresponding to method 2 are reasonable. However, further investigation is needed as to the reasons for the observed discrepancies.

3.3. Major findings

In this chapter, a capacity spectrum method was proposed to determine the performance of HSR columns. The proposed method was used to estimate the performance of HSR columns at DE and MCE hazards. The results obtained with the CSM were compared with nonlinear dynamic analysis. The results of the proposed design method were reasonable when compared to the results from dynamic analysis.

4. SUMMARY, CONCLUSIONS AND SCOPE OF FUTURE WORK

4.1. Summary

In this thesis, a *simplified* model to perform monotonic pushover analysis on HSR columns was derived and validated against experimental data. Next, a more *detailed* and generalized model capable of computing monotonic and cyclic pushover of HSR column was derived. This detailed model – Model 1 – had the curvature at the column bottom as input/control parameter, and its application was only limited to pushover analysis. This model was subsequently modified with the lateral column displacement as input/control parameter – Model 2 – and became suitable for cyclic pushover analyses and for random loading. Using the detailed model, a parametric study on the design variables was conducted. A capacity spectrum design methodology was also proposed to determine the performance of HSR column for a given hazard. This design methodology was verified through an incremental dynamic analysis of a selected HSR column.

4.2. Conclusions

The major findings of this thesis are:

- The pushover analysis from the proposed *simplified* model could predict the response reasonably well, particularly in terms of peak forces. The unloading and residual displacements were under-estimated.
- The monotonic and cyclic pushover results from the *detailed* model were found to better estimate the behavior of HSR columns. The unloading sections and residual displacements were better estimated when compared to the previous model.

- Comparison of the results from the detailed model with the results from past experimental studies showed that the joint sliding behavior was captured reasonably well, despite assuming the sliding response at all joints to be the same.
- Parametric study on the design parameters of HSR columns showed that, the coefficient of friction and the diameter of the duct adaptors control the response characteristics. Specifically, when these parameters are chosen such that sliding is allowed, the HSR columns are observed to be able to accommodate higher displacements without failure.
- The capacity spectrum method proposed in this study can be used to determine the performance of HSR columns fairly well, yet further improvements are needed. By varying the system geometric and material properties (in an iterative manner), economical designs can be explored.

4.3. Scope for future work

On the basis of the findings of this work, suggestions for future research include:

- Incorporate more detailed models for concrete and PT tendon behavior
- Propose a more detailed model, where sliding amplitude in each joint is considered individually.
- Include the effects of friction between the tendon and duct.
- Improve the Capacity Spectrum Method to better capture response of HSR Columns
- Incorporate the capacity spectrum method in an optimization framework to efficiently design for various parameters of HSR columns.

5. REFERENCES

(FEMA), F. E. M. A. (2009). "Quantification of Building Seismic

Performance Factors." *FEMA P695, FEMA, Washington, DC.*

Army, U. (1986). "Seismic Design Guidelines for Essential Buildings." *Departments of the Army (TM-809-10-1), the Navy (NAVFAC P355. 1), and the Air Force (AFM 88-3, Chap. 13, Sect. A), Washington, DC*.

ASCE (2010). *Minimum Design Loads for Buildings and Other Structures: Second Printing*, American Society of Civil Engineers.

Bertero, V. (1995). "Tri-service manual methods in vision 2000." Part.

Casarotti, C., Pinho, R. (2007). "An adaptive capacity spectrum method for assessment of bridges subjected to earthquake action." *Bulletin of Earthquake Engineering*, 5(3): 377-390.

Chopra, A. K., Goel, R. K. (1999). "Capacity-demand-diagram methods for estimating seismic deformation of inelastic structures: SDF systems." *Civil and Environmental Engineering*: 53.

Chou, C. C., Chen, Y. C. (2006). "Cyclic tests of post-tensioned precast CFT segmental bridge columns with unbonded strands." *Earthquake engineering & structural dynamics*, 35(2): 159-175.

Czarnecki, R. M., Freeman, S.A. and Scholl, R.E. (1975). "Destructive Test of a 4-Story Concrete

Structure." *Proceedings of Fifth European Conference on Earthquake Engineering, Istanbul, Turkey*.

ElGawady, M. A., Dawood, H. M. (2012). "Analysis of segmental piers consisted of concrete filled FRP tubes." *Engineering Structures*, 38: 142-152.

FEMA, F. (2009). "P695-Quantification of Building Seismic Performance Factors, Federal Emergency Management Agency (FEMA), Document No." FEMA.

Freeman, S., Nicoletti, J., Tyrell, J. "Evaluations of existing buildings for seismic risk–A case study of Puget Sound Naval Shipyard, Bremerton, Washington." *Proc., Proceedings of the 1st US National Conference on Earthquake Engineering*, Earthquake Engineering Research Institute Oakland, CA, 113-122.

Freeman, S., Honda, K., Blume, J. "Dynamic Response Investigations of Real Buildings." *Proc., Proceedings of Workshop on Earthquake-Resistant Reinforced Concrete Building Construction, University of California, Berkeley, USA*.

Freeman, S., Nicoletti, J., Matsumura, G. "Seismic design Guidelines for essential buildings." *Proc., Memorias del VIII World Conference on Earthquake Engineering, EERI*, 715-722.

Freeman, S. A., Chen, C., Czarnecki, R. (1976). "Dynamic response characteristics of reinforced concrete structures." Blume (John A.) and Associates, Engineers, San Francisco, Calif.(USA).

Freeman, S. A. (1978). "Prediction of response of concrete buildings to severe earthquake motion." *Special Publication*, 55: 589-606.

Freeman, S. A. "Code designed steel frame performance characteristics." *Proc., Dynamics of Structures*, ASCE, 383-396.

Freeman, S. A. "The capacity spectrum method as a tool for seismic design." *Proc., Proceedings of the 11th European conference on earthquake engineering*, Citeseer, 6-11.

Freeman, S. A. (2004). "Review of the development of the capacity spectrum method." *ISET Journal of Earthquake Technology*, 41(1): 1-13.

Harajli, M. H. (2010). "Proposed modification of AASHTO-LRFD for computing stress in unbonded tendons at ultimate." *Journal of Bridge Engineering*, 16(6): 828-838.

Hewes, J. T., Priestley, M. N. (2002). "Seismic design and performance of precast concrete segmental bridge columns."

Hewes, J. T. (2007). "Seismic tests on precast segmental concrete columns with unbonded tendons." *Bridge Structures*, 3(3-4): 215-227.

Hieber, D. G., Wacker, J. M., Eberhard, M. O., Stanton, J. F. (2005). "Precast concrete pier systems for rapid construction of bridges in seismic regions." *Washington State Department of Transportation Technical Report WA-RD*, 611.

Krawinkler, H. "New trends in seismic design methodology." EUROPEAN CONFERENCE ON EARTHQUAKE ENGINEERING.

Mahaney, J. A., Paret, T. F., Kehoe, B. E., Freeman, S. A., Consortium, U. C. U. S. E. "The capacity spectrum method for evaluating structural response during the Loma Prieta earthquake." *Proc., < 1993= Mil novecientos noventa y tres> National Earthquake Conference: Earthquake Hazard Reduction in the Central and Eastern United States: A Time for Examination and Action*, US Central United States Earthquake Consortium (CUSEC), 501-510.

Mander, J. B., Priestley, M. J., Park, R. (1988). "Theoretical stress-strain model for confined concrete." *Journal of structural engineering*, 114(8): 1804-1826.

Matsumoto, E., Kreger, M., Waggoner, M., Sumen, G. (2002). "Grouted connection tests in development of precast bent cap system." *Transportation Research Record: Journal of the Transportation Research Board*, (1814): 55-64.

Matsumoto, E. E., Waggoner, M. C., Kreger, M. E., Vogel, J., Wolf, L. (2008). "Development of a precast concrete bent-cap system." *PCI journal*, 53(3): 74-99.

Mattock, A. H. (1979). "Flexural strength of prestressed concrete sections by programmable calculator." *PCI journal*, 24(1): 32-54.

Pang, J. B., Eberhard, M. O., Stanton, J. F. (2009). "Large-bar connection for precast bridge bents in seismic regions." *Journal of Bridge Engineering*, 15(3): 231-239.

Paulay, T., Priestley, M. (1992). "Seismic design of concrete and masonry structures." *John Wilev and Sons. New York*.

Pinho, R., Casarotti, C., Antoniou, S. (2007). "A comparison of single-run pushover analysis techniques for seismic assessment of bridges." *Earthquake engineering & structural dynamics*, 36(10): 1347-1362.

Priestley, M., Calvi, G., Kowalsky, M. "Direct displacement-based seismic design of structures." *Proc., 5th New Zealand Society for Earthquake Engineering Conference*.

Priestley, M. N. (1997). "Myths and fallacies in Earthquake Engineering." *Concrete International*, 19(2): 54-63.

Restrepo, J., Tobolski, M., Matsumoto, E. (2011). "NCHRP Report 681-Development of a Precast Bent Cap System for Seismic Regions." *NCHRP 12*, 74.

Restrepo, J. I., Rahman, A. (2007). "Seismic performance of self-centering structural walls incorporating energy dissipators." *Journal of Structural Engineering*, 133(11): 1560-1570.

Roh, H.-S. (2007). *Seismic behavior of structures using rocking columns and viscous dampers*, ProQuest.

Sideris, P. (2012). *Seismic analysis and design of precast concrete segmental bridges*.

Sideris, P., Aref, A. J., Filiatrault, A. (2014a). "Effects of anchorage hardware on the cyclic tensile response of unbonded monostrands." *PCI J*, 59(3): 60-77.

Sideris, P., Aref, A. J., Filiatrault, A. (2014b). "Large-scale seismic testing of a hybrid sliding-rocking posttensioned segmental bridge system." *Journal of Structural Engineering*, 140(6): 04014025.

Sideris, P., Aref, A. J., Filiatrault, A. (2014c). "Quasi-static cyclic testing of a large-scale hybrid sliding-rocking segmental column with slip-dominant joints." *Journal of Bridge Engineering*, 19(10): 04014036.

Specifications, A. L. B. D. (2007). "AASHTO LRFD Bridge Design

Specifications, 4th Edition." *American Association of State Highway and Transportation*

Officials (AASHTO), 444 North Capitol Street, NW, Suite 249, Washington, DC 20001.

Standardization, E. C. f. (1994). "Eurocode 8: Design Provisions for Earthquake Resistance of Structures." *Central Secretariat,*

CEN, Brussels.

Stanton, J., Eberhard, M. "Accelerating bridge construction in regions of high seismicity." *Proc., Proc., Special Int. Workshop on Seismic Connection Details for Segmental Bridge Construction, Tech. Rep. No. MCEER-09*.

Steuck, K. P., Eberhard, M. O., Stanton, J. F. (2009). "Anchorage of large-diameter reinforcing bars in ducts." *ACI Structural Journal*, 106(4): 506.